

Research Article

# Mitofusins modulate the increase in mitochondrial length, bioenergetics and secretory phenotype in therapy-induced senescent melanoma cells

Jennyfer Martínez<sup>1</sup>, Doménica Tarallo<sup>1</sup>, Laura Martínez-Palma<sup>2</sup>, Sabina Victoria<sup>3</sup>, Mariana Bresque<sup>4</sup>, Sebastián Rodríguez-Bottero<sup>2</sup>, Inés Marmisolle<sup>1</sup>, Carlos Escande<sup>4</sup>, Patricia Cassina<sup>2</sup>, Gabriela Casanova<sup>5</sup>, Mariela Bollati-Fogolin<sup>3</sup>, Caroline Agorio<sup>6</sup>, María Moreno<sup>7</sup> and  Celia Quijano<sup>1</sup>

<sup>1</sup>Centro de Investigaciones Biomédicas (CEINBIO) and Departamento de Bioquímica, Facultad de Medicina, Universidad de la República, Montevideo, Uruguay; <sup>2</sup>Departamento de Histología y Embriología, Facultad de Medicina, Universidad de la República, Montevideo, Uruguay; <sup>3</sup>Cell Biology Unit, Institut Pasteur de Montevideo, Montevideo, Uruguay; <sup>4</sup>Metabolic Diseases and Aging Laboratory, Institut Pasteur de Montevideo, Montevideo, Uruguay; <sup>5</sup>Unidad de Microscopía Electrónica de Transmisión, Facultad de Ciencias, Universidad de la República, Montevideo, Uruguay; <sup>6</sup>Cátedra de Dermatología, Hospital de Clínicas Manuel Quintela, Facultad de Medicina, Universidad de la República, Montevideo, Uruguay; <sup>7</sup>Laboratory for Vaccine Research, Departamento de Desarrollo Biotecnológico, Instituto de Higiene, Facultad de Medicina, Universidad de la República, Montevideo, Uruguay

**Correspondence:** Celia Quijano (celiq@fmed.edu.uy; celia.quijano@gmail.com)



Cellular senescence is an endpoint of chemotherapy, and targeted therapies in melanoma and the senescence-associated secretory phenotype (SASP) can affect tumor growth and microenvironment, influencing treatment outcomes. Metabolic interventions can modulate the SASP, and an enhanced mitochondrial energy metabolism supports resistance to therapy in melanoma cells. Herein, we assessed the mitochondrial function of therapy-induced senescent melanoma cells obtained after exposing the cells to temozolomide (TMZ), a methylating chemotherapeutic agent. Senescence induction in melanoma was accompanied by a substantial increase in mitochondrial basal, ATP-linked, and maximum respiration rates and in coupling efficiency, spare respiratory capacity, and respiratory control ratio. Further examinations revealed an increase in mitochondrial mass and length. Alterations in mitochondrial function and morphology were confirmed in isolated senescent cells, obtained by cell-size sorting. An increase in mitofusin 1 and 2 (MFN1 and 2) expression and levels was observed in senescent cells, pointing to alterations in mitochondrial fusion. Silencing mitofusin expression with short hairpin RNA (shRNA) prevented the increase in mitochondrial length, oxygen consumption rate and secretion of interleukin 6 (IL-6), a component of the SASP, in melanoma senescent cells. Our results represent the first in-depth study of mitochondrial function in therapy-induced senescence in melanoma. They indicate that senescence increases mitochondrial mass, length and energy metabolism; and highlight mitochondria as potential pharmacological targets to modulate senescence and the SASP.

Received: 22 May 2019  
Revised: 8 August 2019  
Accepted: 19 August 2019

Accepted Manuscript online:  
20 August 2019  
Version of Record published:  
10 September 2019

## Introduction

Cellular senescence is a persistent proliferation arrest that can be triggered by many stress stimuli, including telomere attrition, oncogene activation and DNA damage [1]. Senescence is considered a major impediment for tumor genesis and neoplastic transformation involves evasion of senescence [2–4]; nevertheless, many tumors retain the ability to senesce [5]. In melanoma, inactivation of oncogenes [6–8], restoration of tumor suppressors [9,10], chemotherapeutics such as temozolomide (TMZ) [8,11], targeted therapies (e.g. vemurafenib, trametinib, palbociclib) [10,12,13] and radiation [12] can

induce senescence confirming the importance of the pathway. Thus, cellular senescence can be considered a new ‘end point’ of melanoma therapy alternative to death by apoptosis or mitotic catastrophe [14,15].

In senescent cells, proliferation arrest involves the increase in cyclin-dependent kinase inhibitor 2A (p16-INK4), and/or tumor suppressor p53 that promotes the transcription of cyclin-dependent kinase inhibitor 1 (p21). Both p16 and p21 prevent the phosphorylation of the retinoblastoma protein (pRb), repressing E2F transcription factor activity, needed for S-phase entry in the cell cycle [1,16]. Senescent cells present changes in cell morphology, increase in lysosomal  $\beta$ -galactosidase activity, activation of the DNA damage response, heterochromatin foci and a secretory phenotype of growth factors, cytokines and proteases, known as the senescence-associated secretory phenotype (SASP) [1].

While the arrest in the proliferation of senescent cells is clearly tumor suppressive, the impact of the SASP on the tumor microenvironment is diverse, and depends on the cell type, the inducer of senescence and the tissue where the SASP exert its effects [17,18]. Recent work shows that targeted apoptosis of senescent cells reduces breast cancer relapse and metastasis after chemotherapy and prevents fatigue and cardiotoxicity [19]. However, both pro- and anti-tumor effects have been reported for the senescent secretome in melanoma; [8,20–23]; and it is still not clear if senescence is a beneficial or detrimental response to cancer therapy [24].

Senescent cells also present profound alterations in their energy metabolism and a shift towards energy-producing pathways at the expense of biosynthetic routes has been observed [25]. In particular, an increase in mitochondrial oxygen consumption and oxidative phosphorylation has been reported in oncogene-induced senescence in human fibroblasts [26–28] and in therapy-induced senescence in lymphoma [29]. However, in replicative and DNA damage-induced senescence, an impairment of mitochondrial function and increased glycolysis and glucose fermentation to lactate has been described [30–32]. Thus, senescent cells appear to have different bioenergetic phenotypes, depending on the triggering stimuli.

Most of what we know about the metabolism of the senescent cell comes from research carried out in fibroblasts, while relatively little is known about the metabolism of melanoma senescent cells. However, increasing evidence supports a role for mitochondria in resistance to therapy in melanoma [33–36] and mitochondrial metabolism appears as a plausible target to overcome resistance to targeted therapies [36].

Mitochondrial energy metabolism relies heavily on fusion, fission, biogenesis and mitophagy. These events play a role in the quality control of the organelle and adaptation to the energy demands [37,38]. In particular, fusion and fission proteins MFN1, MFN2, optic atrophy protein 1 homolog (OPA1), dynamin-related protein 1 (DRP1), mitochondrial fission factor (MFF) and mitochondrial fission 1 protein (FIS1), modulate mitochondrial shape in response to cellular requirements [37,38].

We hypothesized that the phenotypic changes experienced by the senescent cells, in particular, proliferation arrest and increased synthesis and secretion of components of the SASP, would lead to changes in cell metabolism and bioenergetics that would impact mitochondria. Thus, in this work we explored the alterations in mitochondrial metabolism that accompany the induction of senescence in mouse melanoma cells exposed to TMZ, an alkylating agent used in chemotherapy [39]. Our results show that TMZ leads to an increase in several mitochondrial respiratory parameters; along with changes in both mitochondrial mass and length. Furthermore, we identify mitochondrial fusion proteins that are required for the establishment of the SASP during chemotherapy against melanoma.

## Experimental

### Cell culture and treatment

The mouse melanoma B16-F1 cell line (CRL-6323, ATCC) was cultured in Dulbecco’s modified Eagle’s medium (DMEM, Gibco) with 4.5 g/l glucose, 10% FBS (Gibco), penicillin 50 U/ml and streptomycin 50  $\mu$ g/ml. All cells were maintained at 37°C in a CO<sub>2</sub> incubator (95% air, 5% CO<sub>2</sub>). All reagents were from Sigma unless otherwise specified.

B16-F1 cells were treated with 200  $\mu$ M TMZ for 5 h, this procedure was performed twice with a 24-hour interval. Treatment with the vehicle, dimethyl sulfoxide (DMSO), was used as control in all experiments. Measurements were made 4 days after the second exposure to the drug, unless otherwise specified.

### Senescence-associated $\beta$ -galactosidase (SA- $\beta$ -gal) assay

Cells were stained as described previously [40]. Percentage positive staining was calculated by counting at least 100 random cells in five different microscopic fields.

## Mitochondrial mass and morphology in living cells

Cells were incubated, in the culture medium without serum, with 300 nM MitoTracker Green FM (Thermo Fisher Scientific) at 37°C for 30 min. Mitochondrial mass was assessed by flow cytometry (BD FACSCalibur), measuring geometrical mean fluorescence intensity of the population.

Mitochondrial length was determined using ImageJ software. The threshold fluorescence was adjusted, binary images generated and the *Feret's diameter* (longest distance between any two points along the selection boundary) [41] of selected particles determined. The analysis was limited to regions in the periphery of cells, where individual mitochondria were easily resolved, since in the perinuclear region of the cell the high density of mitochondria prevented determining the size of each mitochondria [42–45]. At least three different microscope slides, obtained from different cultures, were analyzed for each condition, and more than 4000 mitochondria per slide were evaluated in different microscopic fields. Mean values of mitochondrial length were determined considering all measured mitochondria in each slide. Frequency distribution analyses were performed in 4000 mitochondria per condition, picked randomly from all the measurements obtained in different slides, a bin width of 0.5 was chosen.

## Cellular bioenergetics

Oxygen consumption rate (OCR) and extracellular acidification rate (ECAR) were measured simultaneously in a Seahorse XFe24 extracellular flux analyzer (Agilent). Before the experiment, the culture medium was replaced with an unbuffered medium (DMEM pH 7.4, supplemented with 5 mM glucose, 1 mM sodium pyruvate, 32 mM NaCl and 2 mM glutamine) and incubated for 1 h at 37°C without CO<sub>2</sub>. Basal oxygen consumption measurements were taken before the injection of oxidative phosphorylation inhibitors or an uncoupler. For mitochondrial respiratory analysis, successive measurements were taken after the sequential addition of oligomycin (1 μM), carbonyl cyanide 4-(trifluoromethoxy)phenylhydrazone (FCCP, 1.5 μM, two additions) and antimycin A (AA, 0.5 μM) [46].

Respiration in permeabilized cells was measured after the addition of digitonin (40 μg/ml, Applichem) [47]. Briefly, the concentration of digitonin was titrated to assure that the plasma membrane was permeabilized, without affecting mitochondrial integrity. OCR was determined using pyruvate (5 mM)/malate (2.5 mM) and succinate (10 mM), specific substrates of mitochondrial electron transport complexes I and II, respectively. We performed measurements in the absence and presence of ADP (1 mM) to determine mitochondrial respiration in state 2 and state 3, respectively [47,48]. Respiratory control ratios (RCR) were calculated as the ratio between state 3 and state 2, assuming that state 2 respiration would be very similar to state 4 since in the absence of contaminating ATPases both rates are mainly controlled by proton leak [48].

Antimycin A-resistant respiration (non-mitochondrial respiration) was subtracted from all oxygen consumption measurements. After each assay, protein content (μg) per well was determined with the bicinchoninic acid (BCA) technique (Pierce, Thermo Scientific) or cells were detached with Trypsin-EDTA and counted with a Z1 Coulter Counter Dual Threshold (Beckman Coulter). OCRs and ECARs were normalized considering either protein content (μg) or cell number.

To study glucose fermentation to lactate, the ECAR was measured before (ECAR<sub>basal</sub>) and after the addition of 80 mM oxamate (ECAR<sub>Ox</sub>) or 80 mM 2-deoxyglucose (ECAR<sub>2-DG</sub>), inhibitors of lactate dehydrogenase and hexokinase, respectively [49]. To determine how much of the ECAR was affected by the hexokinase inhibitor, and was due to glucose catabolism in glycolysis, we calculated the fraction of the ECAR that was sensitive to 2-DG (see eqn 1). Similarly, we determined the fraction of extracellular acidification depending on lactate formation (see eqn 2).

$$\text{ECAR sensitive to 2-DG} = \frac{\text{ECAR}_{\text{basal}} - \text{ECAR}}{\text{ECAR}_{\text{basal}}} \quad (1)$$

$$\text{ECAR sensitive to oxamate} = \frac{\text{ECAR}_{\text{basal}} - \text{ECAR}_{\text{Ox}}}{\text{ECAR}_{\text{basal}}} \quad (2)$$

## Immunofluorescence

Cells were cultured in glass slides or coverslips, fixed in 4% paraformaldehyde, permeabilized with 0.1% Triton in PBS, incubated in blocking buffer (3% BSA, 0.1% Triton in PBS) for 1 h and incubated with primary

antibodies overnight at 4°C. The following day cells were incubated with the secondary antibodies: Alexa Fluor® 488 goat anti-rabbit IgG (H + L) (#A11034) and Alexa Fluor® 594 goat anti-mouse IgG (H + L) (#A11005) from Thermo Fisher Scientific and 4',6-diamidino-2-phenylindole (DAPI, 1 µg/ml, Thermo Fisher Scientific) was used to stain the nuclei.

For the detection of phosphorylated histone H2AX (γ-H2AX) foci, we used a primary antibody anti-γ-H2AX (Ser139) (Millipore #07-164, 1:2000). Cells were imaged by a epifluorescence microscopy (Nikon Eclipse TE200). Percentage positive staining was calculated counting cells with foci formation in more than 100 random cells in five different fields.

For proliferation assays, cells were incubated with bromodeoxyuridine (BrdU, 10 µM, BD Pharmingen) for 6 h, fixed with cold methanol at –20°C for 5 min and washed with PBS. The slides were treated with HCl 2N, Triton 0.5% in PBS for 20 min, washed with PBS to neutralize HCl. Cells were then incubated in blocking buffer, followed by incubation with an anti-BrdU antibody (#347580 Becton Dickinson, 1 : 50). Cells were imaged by the epifluorescence microscopy (Nikon Eclipse TE200). The percentage positive staining was calculated by counting BrdU-stained nuclei in more than 100 random cells in five different fields. For the evaluation of *Mfn1* silencing, we used a primary antibody anti-MFN1 (ab104274 Abcam 1 : 100) and imaged by epifluorescence microscopy (Nikon Eclipse TE200).

For colocalization assays, cells were immunostained with the primary antibodies anti-SDH subunit A (ab14715 Abcam 1 : 200) and anti-DRP1 (ab54038, Abcam 1 : 200) and imaged by confocal microscopy (Leica, SP5). Pearson correlation coefficient [50] was determined with the Icy free software using the Colocalization Studio plugin. This coefficient is independent of signal because it subtracts the mean intensity from each pixel's intensity value [51]. At least three different microscope slides, obtained from different cultures, were analyzed for each condition.

### Assessment of mtDNA/nDNA ratio

Total DNA was extracted from cultured cells with DNAzol reagent following the manufacturer's instructions, extending the precipitation time to 20 min at –20°C. DNA was quantified measuring  $A_{260\text{ nm}}$  and the purity of the samples controlled measuring  $A_{260}/A_{280}$  ratio with a NanoDrop (Thermo Fisher Scientific). PCR primer sequences for murine mitochondrial encoded gene 12S rRNA: 5'-ACCGCGGTCATACGATTAAC-3' (forward) and 5'-CCCAGTTTGGGTCTTAGCTG-3' (reverse); and nuclear encoded target 18S rRNA: 5'-CGCGGTTCTATTTTGTGGT-3' (forward) and 5'-AGTCGGCATCGTTTATGGTC-3' (reverse) were obtained from [52]. Equal amounts of total isolated genomic DNA (15 ng) were used for amplification by real-time quantitative PCR with QuantiTect® SYBR® Green PCR Kit (Qiagen) and 0.5 µM of each primer in a Rotor-Gene 6000 analyzer (Corbett). Separate tubes were used for mtDNA and nDNA amplification. The mtDNA/nDNA ratio was calculated as  $2^{(C_{\text{tn}} - C_{\text{mt}})}$ , assuming a doubling of DNA copy per cycle, and results were expressed as fold change relative to control condition [52].

### Flow cytometry analysis and cell sorting of senescent cells

The cells were trypsinized, collected in the culture medium and immediately used for analysis in a BD FACSCalibur flow cytometer (BD Biosciences). Cellular size and granularity were analyzed in the forward and side scatter (FSC-H and SSC-H), respectively. Populations of senescent cells were detected at higher values of both FSC-H and SSC-H as compared with proliferating cultures of melanoma cells, as described previously [53].

Cell sorting was performed using a BD FACSARIA™ Fusion cell sorter (BD Biosciences) equipped with a solid-state diode 488 nm laser. The analysis of the following parameters was carried out with DIVA software: forward-angle light scatter area (FSC-A), sideward scatter area (SSC-A). For doublet discrimination, the analysis of FSC-A versus FSC-H was performed. Cells were sorted using a 70-µm nozzle at a rate of 10 000 events per seconds. The sorting mode was Purity. Sort decision was based on the following gate strategies: FSC-A versus SSC-A dot plot to identify senescent (large) and non-senescent (small) cell populations; and FSC-A versus FSC-H dot plot to exclude doublets.

Following sorting, cells were washed, suspended in the culture medium and plated into tissue culture dishes. SA-β-gal staining and oxygen consumption assays were performed 7 days after sorting. For real-time RT-PCR, RNA was extracted immediately after cell sorting and confocal microscopy was assessed two days after cell sorting.

## Cell size

Cells were detached by incubation with Trypsin-EDTA (0.05%, 0.02%), suspended in PBS and cell diameter measured in Countess™ automated cell counter (Thermo, Fisher Scientific), following the manufacturer's instructions. Cell volume was calculated assuming that cells adopt a spherical shape in suspension ( $V = 4/3\pi r^3$ ).

## Immunoblotting

Cells were routinely lysed in cell lysis buffer containing 20 mM Tris-HCl (pH 7.5), 150 mM NaCl, 0.1% Triton X-100, 1 mM EDTA, 1 mM EGTA, 2.5 mM sodium pyrophosphate, 1 mM  $\beta$ -glycerophosphate, 1 mM  $\text{Na}_2\text{VO}_4$ , 1 mM NaF, 1 mM PMSF, supplemented with Sigma FAST protease inhibitor cocktail and Calbiochem phosphatase inhibitor cocktail. Lysates were sonicated, centrifuged at 10000g for 10 min and stored at  $-80^\circ\text{C}$ . Protein concentration was determined with bicinchoninic acid (Thermo Fisher Scientific). Proteins (20–40  $\mu\text{g}$ ) were resolved by SDS-PAGE and transferred to nitrocellulose membranes at  $4^\circ\text{C}$  overnight using standard Western blotting procedures. The membranes were incubated with primary antibodies overnight at  $4^\circ\text{C}$ . Anti-phospho-ATM (Ser1981) (05-740 1:1000) and anti- $\alpha$ -tubulin (05-829 1:1000) were from Millipore. Anti-ATM (#2873 1:1000), anti-phospho-p53 (Ser15) (#9284 1:1000) and anti-GAPDH (#2118, 1:1000) were from Cell Signaling Technology. Anti-p53 (sc-6243 1:1000) and anti-p21 (sc-397 1:1000) were from Santa Cruz Biotechnology. Anti-OPA1 (ab42364 1:1000), anti-DRP1 (ab54038 1:1000), anti-MFN1 (ab104274 1:4000), anti-MFN2 (ab124773 1:1000), anti-FIS1 (anti-TTC1, ab71498 1:1000), anti-Complex I subunit 8 kDa (ab110245, 1:1000), anti-ATP5A (ab14748, 1:1000), anti-SDHA (ab14715 1:1000), anti-COX IV (ab33985 1:1000), anti-MFF (ab129075, 1:1000) were from Abcam.

Secondary antibodies: IRDye® 800 anti-Rabbit IgG (H + L) (#926-32211, 1:20 000) and IRDye® 680 anti-Mouse IgG (H + L) (#926-68070, 1:20 000) from LI-COR Bioscience were used and immunoblots were visualized with the Odyssey (LI-COR Biosciences) and analyzed with Image Studio Lite (LI-COR Bioscience).

## Gene expression analysis

Total RNA was extracted with TRIzol reagent (Thermo Fisher Scientific) and precipitated with isopropanol. The isolated RNA was quantified at  $A_{260\text{ nm}}$  and the purity of the sample controlled measuring  $A_{260}/A_{280}$  ratio in a NanoDrop (Thermo Fisher Scientific). Prior to cDNA synthesis, 1  $\mu\text{g}$  of total RNA was treated with DNase-I (Thermo Fisher Scientific). Retrotranscription was performed in a final volume of 20  $\mu\text{l}$  in the presence of random primers (200 ng), dNTPs (0.5 mM), DTT (0.01 M), RNaseOUT (40 U) and M-MLV Reverse Transcriptase (Invitrogen).

Quantitative RT-PCRs were carried out using QuantiTect® SYBR® Green PCR Kit (Qiagen) with specific primers (Supplementary Material), in a Rotor-Gene 6000 analyzer (Corbett). Beta-Actin encoding gene *Actb* was used as house-keeping gene. The relative mRNA amount in each sample was calculated using the  $2^{-\Delta\Delta\text{Ct}}$  method [54] where  $\Delta\text{Ct} = \text{Ct}_{\text{gene of interest}} - \text{Ct}_{\text{Actb}}$ . Results were expressed as relative fold change in mRNA levels compared with control cells.

## Transmission electron microscopy

Cells from both groups (control and TMZ) were fixed overnight at  $4^\circ\text{C}$  in 3% glutaraldehyde in cacodylate buffer (CB) at pH 7.2. After five successive washings in CB of 5 min each, samples were post-fixed in 1% OsO<sub>4</sub> in Milli Q water for 30 min, followed by five washes of 5 min each. Dehydration was performed in ethanol baths of increasing concentration, followed by acetone. The imbibition of the cells and their inclusion in blocks was performed using Araldite ACM resin of Fluka. The ultrathin sections were made in an RMC-MTX ultramicrotome and collected on 200 mesh copper grids. The contrast was first performed with 2% aqueous uranyl acetate for 30 min at  $60^\circ\text{C}$ , and after with Lead Citrate following the Reynolds protocol. The observation was performed on a Jeol JEM-1010 transmission electron microscope, operating at 100 kW. The images were captured with a HAMAMATSU C-4742-95 digital camera and processed with the Photoimpact program.

Mitochondrial length was determined in the electron microscopy images using the ImageJ software. Lines were traced indicating the longest distance between two points in the organelle and measured using the *Length* parameter.

## Citrate synthase activity

Enzymatic activity of citrate synthase was assessed spectrophotometrically at 412 nm following the reduction in 5,5'-dithio-bis-[2-nitrobenzoic acid] (100  $\mu$ M) in the presence of oxaloacetate (250  $\mu$ M) and acetyl-CoA (50  $\mu$ M) [55].

## Lentiviral shRNA transduction

Plasmids carrying shRNA constructs targeting *Mfn1* (TRCN0000081402 and TRCN0000081398) *Mfn2* (TRCN0000080610) were from Dharmacon. The plasmid-carrying scrambled shRNA was a gift from David Sabatini (Addgene plasmid # 1864[56]); pCMV-VSV-G and pCMV-dR8.2 dvpr were a gift from Bob Weinberg (Addgene plasmids # 8454 and #8455[57]). Lentiviral vectors were produced in 293T cells according to the protocols established by the Broad Institute RNAi Consortium ([www.broadinstitute.org/genome\\_bio/trc/publicProtocols.html](http://www.broadinstitute.org/genome_bio/trc/publicProtocols.html)). B16-F1 cells were transduced with lentiviruses overnight in complete media with 8  $\mu$ g/ml polybrene. Infected cells were subsequently selected in DMEM supplemented with 2  $\mu$ g/ml puromycin.

## Subcellular fractionation

After TMZ treatment, B16-F1 cells were ruptured in homogenization buffer (Tris-HCl 10 mM, 0.25 M sucrose, pH 7.6) with a Potter-Elvehjem homogenizer. Lysates were centrifuged at 1000g for 10 min at 4°C to remove whole cells and nuclei. Mitochondrial and cytosol-enriched fractions were obtained by centrifugation at 14000g for 10 min at 4°C. The supernatant was enriched in cytosolic proteins and the pellet in mitochondria. The pellet was washed with homogenization buffer and then resuspended in Tris-HCl 10 mM, pH 7.6 with a protease inhibitor. Protein concentration was determined by the BCA method.

## ELISA

Cells were seeded in six-wells plates and three days after TMZ treatment cells were washed with PBS and added 1 ml of DMEM. Two days after the medium was collected, centrifuged at 1000g to remove cells and debris and stored at -80°C. IL-6 cytokine analysis was assessed by ELISA using OptEIA™ Set kit (BD Bioscience). Results were normalized to  $\mu$ g of protein.

## Statistical analysis and graphs

All plots and statistical analysis were performed using GraphPad Prism. Data were analyzed by two-tailed unpaired or paired Student's *t*-test, as appropriate, (when comparing two groups); or one- or two-way ANOVA with Tukey post hoc tests, as appropriate, (when comparing more than two groups). Frequency distributions were analyzed performing contingency tables and Chi-square tests [58]. *P* < 0.05 was considered statistically significant. Scatter dot plots are used in most cases, bar plots are shown in experiments with *n* > 8. In all cases, results in the text show mean  $\pm$  S.D. In all experiments, *n* values represent the number of independent biological samples (wells, culture dishes or coverslips per group/condition). All experiments and statistical analysis were performed with *n*  $\geq$  3.

## Results

### TMZ induces senescence in melanoma cells

To study the metabolic alterations that accompany the induction of senescence in melanoma, we established a model of therapy-induced senescence. We exposed B16-F1 mouse melanoma cells to TMZ, a genotoxic agent used in chemotherapy whose mechanism of action involves the methylation of O6-guanine residues in DNA [39]. B16-F1 cells lack cyclin-dependent kinase inhibitor p16-INK4 and present wild-type p53 [59], thus are good candidates to induce senescence through the activation of the DNA damage response and p53/p21 pathway.

Exposure of B16-F1 cells to two additions of TMZ, in concentrations similar to those found in the blood of patients undergoing chemotherapy [60,61], led to the persistent activation of the DNA damage response. Phosphorylation and activation of the DNA damage sensor ataxia-telangiectasia mutated kinase (ATM), and of its substrate p53 could be observed in the culture after treatment (Figure 1A), along with an increase in p53 and p21 levels (Figure 1A). Quantitation of p21 mRNA showed a gradual increase, achieving a sevenfold increase after 4 days of exposure to the drug (Supplementary Fig. S1A). Activation of the DNA damage

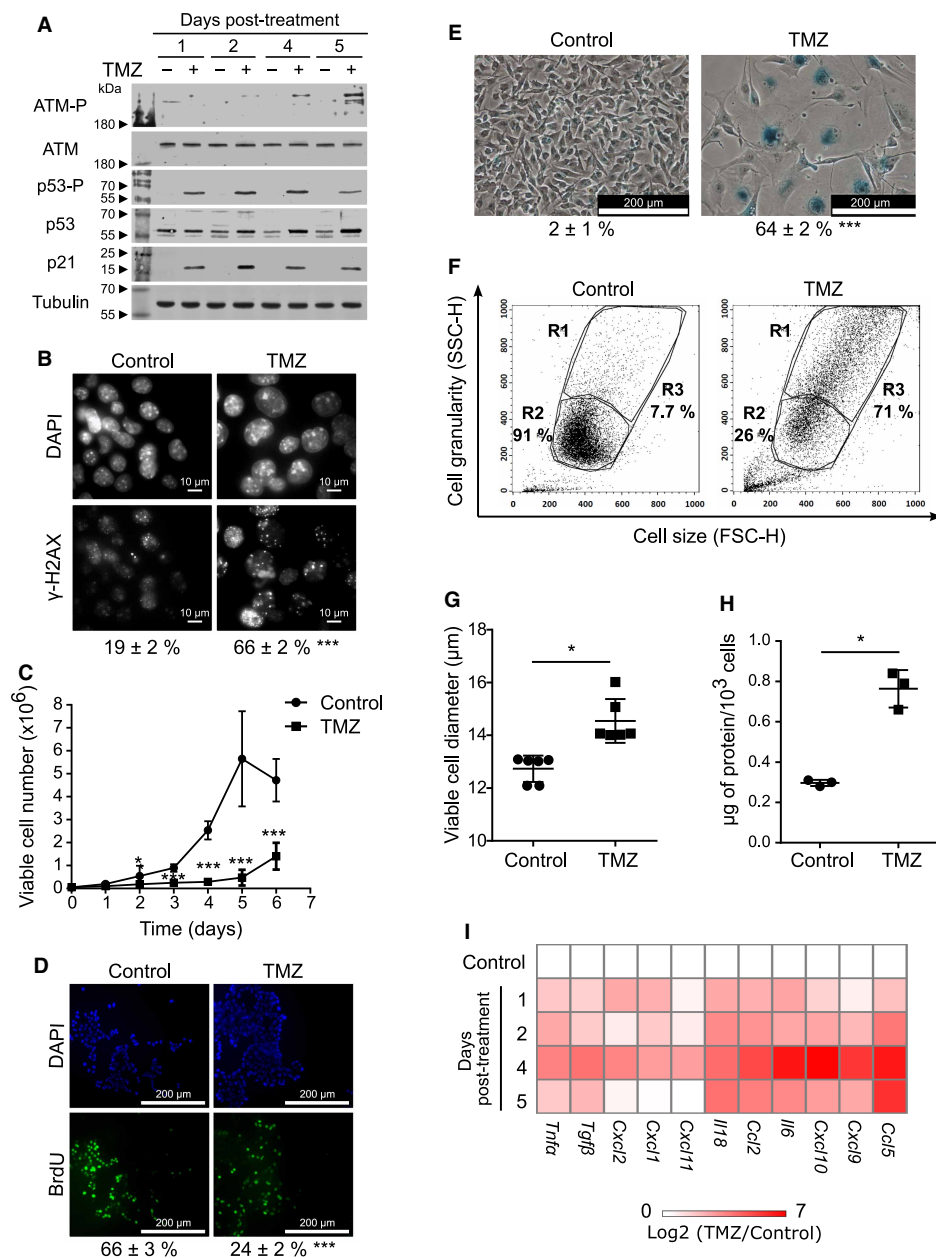


**Figure 1. TMZ induces senescence in mouse melanoma cells.**

Part 1 of 2

B16-F1 cells were exposed twice to TMZ (200 μM) or the vehicle, DMSO (Control) for 5 h with a 24 h interval. Measurements were performed at different times after the second exposure to the drug. **(A)** Representative western blots performed with antibodies for phosphorylated ATM (Ser1981) (ATM-P), ATM, phosphorylated p53 (Ser15) (p53-P), p53, p21 and tubulin ( $n = 3$  culture dishes per condition). **(B)** Representative images of  $\gamma$ -H2AX nuclear foci two days after TMZ treatment. The percentage of cells with nuclear foci is shown below the picture ( $n = 6$  coverslips per group). **(C)** Growth curves were obtained counting live cells by trypan blue exclusion ( $n = 9$  wells per group). **(D)** Representative images of BrdU incorporation to DNA. The percentage of cells with positive nuclear staining is shown below the picture ( $n = 6$  coverslips per group). **(E)** Representative images of SA- $\beta$ -gal activity assay four days after TMZ exposure. The percentage of positive cells is shown below the picture ( $n = 6$  wells per group). **(F)** Cell size (FSC-H parameter) and granularity (SSC-H parameter) were assessed by flow cytometry 4 days after treatment. A representative image is shown ( $n = 3$  wells per group). **(G)** Viable cell diameter of trypsin-detached cells was determined from the histograms in Supplementary Figure S1B ( $n = 6$  culture dishes per group). **(H)** Trypsin-detached cells were counted and protein mass ( $\mu$ g) was determined by the bicinchoninic acid technique ( $n = 3$  culture dishes per group).

**Figure 1. TMZ induces senescence in mouse melanoma cells.**

Part 2 of 2

(I) Real-time RT-PCR was performed for several components of the SASP. Results are expressed relative to the control condition ( $n = 3$  culture dishes per group). Results are the mean  $\pm$  S.D. *T*-tests were performed, \*  $P < 0.05$ , \*\*\*  $P < 0.0001$ .

response was observed 24 h after the second exposure to TMZ and persisted for at least 5 days (Figure 1A). ATM activation also led to an increase in  $\gamma$ -H2AX nuclear foci in treated cells (Figure 1B).

TMZ treatment affected culture growth (Figure 1C) and the arrest in proliferation of melanoma cells was confirmed assessing the incorporation of the thymidine analog BrdU into DNA (Figure 1D). An induction of SA- $\beta$ -gal activity, an increase in size and marked morphological changes could be observed in B16-F1 cells, 4 days after the exposure to TMZ (Figure 1E).

The increase in cell size, along with changes in granularity of the population, was also observed by flow cytometry. TMZ-treated cells presented higher forward and side scatter (FSC and SSC) values than control cells. To determine the percentage of cells that experienced these morphological alterations, the population (R1) was distributed into two different subpopulations (R2 and R3);  $71 \pm 1\%$  of the cells exposed to TMZ could be found in region R3 (larger and more granular cell population) while only  $7.7 \pm 0.5\%$  of control cells were included in this group (Figure 1F).

To quantify the changes in size, cells were detached from the culture dishes and analyzed in the Countess™ automated cell counter. An increment in cell diameter was observed in TMZ-treated cells ( $14.5 \pm 0.3 \mu\text{m}$ ) with respect to control cells ( $12.7 \pm 0.2 \mu\text{m}$ ) (Figure 1G and Supplementary Fig. S1B), that corresponded with nearly 50% increase in cell volume (control cells  $1100 \pm 100 \mu\text{m}^3$  and TMZ-treated cells  $1600 \pm 300 \mu\text{m}^3$ ). Measurement of protein mass per cell revealed a 2.6-fold increase in treated cells with respect to control cells (Figure 1H) that clearly exceeded the increment in volume.

Evaluation of mRNA levels of various cytokines and growth factors revealed an increase in interleukins 6 and 18 (*Il-6*, and *Il-18*), chemokine (C-C motif) ligands 2 and 5 (*Ccl2*, *Ccl5*), chemokine (C-X-C motif) ligand 9, 10 and 11 (*Cxcl9*, *Cxcl10*, *Cxcl11*), interleukin 8 homologs *Cxcl1* and *Cxcl2*, tumor necrosis factor  $\alpha$  (*Tnf $\alpha$* ), and transforming growth factor  $\beta$  (*Tgf $\beta$* ) (Figure 1I). Many of these proteins have already been described as components of the senescent secretome in melanoma [8,20,21,23] confirming the acquisition of a SASP in B16-F1 melanoma cells exposed to TMZ. Cytokine and growth factor gene expression peaked four days after the exposure to the drug (Figure 1I). Together our results show that treatment with TMZ-induced senescence in 60–70% of cells in the culture.

### TMZ-induced senescent cells present increased mitochondrial respiration

Previous reports by others and us have shown that the induction of senescence can be accompanied by profound changes in energy metabolism that differ greatly depending on the cell type and triggering stimuli [26,27,29–32]. Thus, we sought to assess mitochondrial function in TMZ-induced senescence in our melanoma cell model.

We measured real-time OCR in intact cells, using a Seahorse XFe24 extracellular flux analyzer (Agilent), before and after the addition of inhibitors and an uncoupler of the respiratory chain and oxidative phosphorylation (Figure 2A). We found that basal respiration (which occurs in the absence of mitochondrial inhibitors and represents the sum of all mitochondrial oxygen-consuming processes) and respiration linked to ATP synthesis (OCR sensitive to the addition of ATP-synthase inhibitor oligomycin) were higher in senescent cells (Figure 2A,B), while ATP-independent respiration (oligomycin-resistant respiration) was not significantly different between cultures (Figure 2A,B). These results suggest that senescent cells synthesize more ATP in the mitochondria than their non-senescent counterparts. The maximum respiration rate, obtained after titration with the mitochondrial uncoupler FCCP, was substantially increased as well in TMZ-treated cells (Figure 2A,B), indicating that senescent melanoma cells might have more mitochondria than non-senescent cells and/or that their mitochondria present increased activity. Finally, an increase in non-mitochondrial OCR could be appreciated in treated cells (Figure 2B), after the addition of antimycin A, which could be due to the increased activity of NADPH oxidases [62,63].

To evaluate if the increase in respiratory parameters observed in Figure 2A was linked solely to the increase in mass and size of senescent cells, we calculated the coupling efficiency, spare respiratory capacity and RCR (Table 1). These respiratory indexes are determined as ratios between the respiratory rates obtained in different

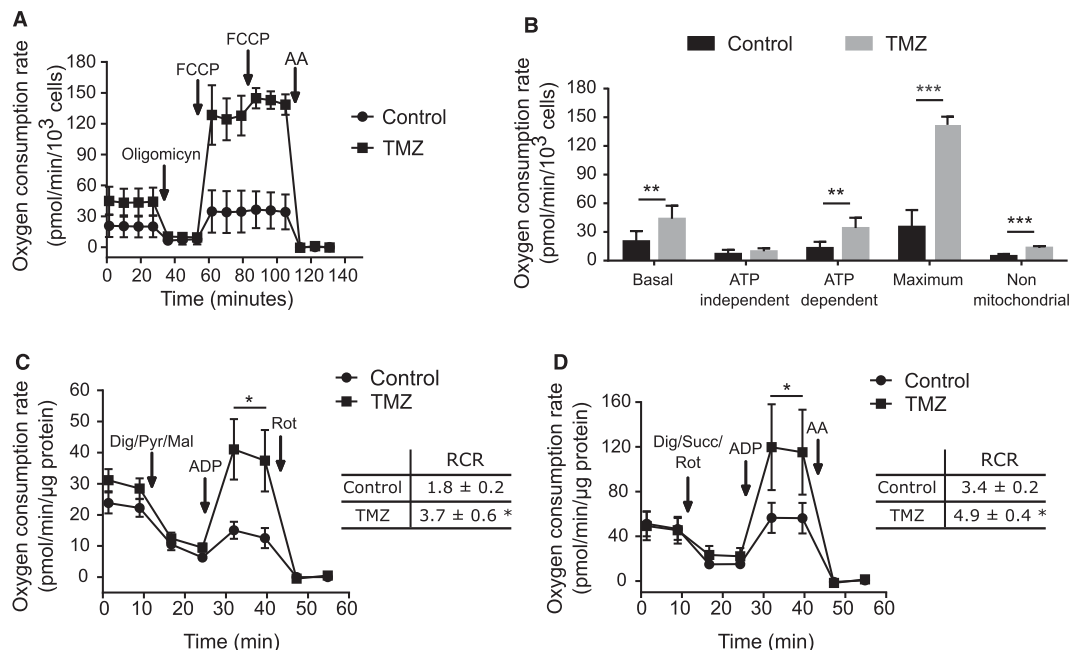


**Figure 2. TMZ-induced senescent cells present increased mitochondrial respiration.**

(A) The oxygen consumption rate (OCR) was determined before and following the sequential addition of oligomycin, FCCP and antimycin A (AA) ( $n=9-10$  wells per group). (B) The graph shows the respiratory parameters obtained from oxygen consumption rate (OCR) measurements in (A). (C and D) Respiration was evaluated in permeabilized cells after the sequential addition of (C) digitonin/pyruvate/malate, ADP, and rotenone; or (D) digitonin/succinate/rotenone, ADP and AA. The tables on the right of each figure show the respiratory control ratio (RCR) for each condition, determined as the ratio between the OCRs after and before the addition of ADP ( $n=10-15$  wells per group). In all figures, results are the mean  $\pm$  S.D. *T*-tests were performed, \*  $P < 0.05$ , \*\*  $P < 0.001$ , \*\*\*  $P < 0.0001$ .

conditions and are therefore internally normalized and independent of cell number or protein mass [46]. The coupling efficiency (ratio between respiration linked to ATP synthesis and basal respiration) was significantly higher in senescent cells than in non-senescent cells (Table 1), indicating that electron transport in mitochondria is more tightly coupled to ADP phosphorylation. The spare respiratory capacity (ratio between the maximum and basal respiration rates) was also higher in treated cells (Table 1), indicating an increase in the ability to respond to energy demands. Finally, the RCR (ratio between maximum and oligomycin-resistant respiration rates) was higher in senescent than non-senescent cells (Table 1) in agreement with an overall enhancement of mitochondrial function upon the induction of senescence.

We also normalized OCR by protein content (Supplementary Figure S2A), to verify if the increase in respiration rate per cell was only due to an increase in mitochondrial content that accompanied the increase in cell size and mass observed in Figure 1. As shown in Supplementary Figure S2A, the maximum respiration rate was

**Table 1 Mitochondrial respiratory ratios of senescent cells**

Respiratory ratios	Control	TMZ
Coupling efficiency	0.67 $\pm$ 0.04	0.77 $\pm$ 0.03 ***
Spare respiratory capacity	1.6 $\pm$ 0.2	3.4 $\pm$ 0.7 ***
Respiratory control ratio	4.9 $\pm$ 0.7	15 $\pm$ 4 ***

Coupling efficiency, spare respiratory capacity and respiratory control rate were calculated from OCR measurements in Figure 2A. Results are the mean  $\pm$  S.D. ( $n=9-10$  wells per group). *T*-test \*\*\*  $P < 0.0001$ .

higher in TMZ-treated cells than control cells, showing that the increase in mitochondrial function surpasses the increase in cell mass.

To rule out that the differences in respiration rates were due to the changes in catabolic routes upstream from mitochondria (e.g. glucose uptake and glycolysis), we measured oxygen consumption in permeabilized cells (Figure 2C,D). The plasma membrane was permeabilized, without affecting the mitochondrial membrane, by the controlled addition of digitonin [47]. Mitochondrial respiration in state 2 was obtained by providing specific substrates for mitochondrial complexes: pyruvate and malate for complex I and succinate for complex II. Respiration in state 3 was determined after the addition of ADP. State 3 respiration and RCRs were significantly higher in senescent than non-senescent cells, for both complex I and II substrates (Tables in Figure 2C,D). These results indicate that mitochondria of senescent cells exhibit enhanced electron transport and coupling and consequently are more efficient in terms of harnessing the energy released during substrate oxidation to synthesize ATP than mitochondria from control cells.

### TMZ-induced senescence in melanoma reduces glucose catabolism to lactate

In the light of the prominent increase in mitochondrial function, we reasoned that the main catabolic pathways would probably change upon the induction of senescence. We looked for alterations in the glycolytic pathway by measuring the ECAR. As lactate is excreted from the cell in co-transport with  $H^+$ , a decrease in extracellular pH can indicate an increase in glucose catabolism to lactate [49]. Basal ECAR of control cells was higher than that of senescent cells (Figure 3A,C). To discriminate acidification due to lactate formation from that caused by other acids, we determined the fraction of basal extracellular acidification that was sensitive to a pharmacological inhibitor of hexokinase, (2-deoxyglucose, 2-DG), and of lactate dehydrogenase (oxamate) (Figure 3B,D, respectively). The addition of 2-DG [49] significantly reduced ECAR in both senescent and non-senescent cells (Figure 3A). In fact, a relevant fraction of the acidification rate (>0.70) was sensitive to the hexokinase inhibitor in both conditions (Figure 3B). Conversely, the addition of oxamate [49] decreased the ECAR of control cells,

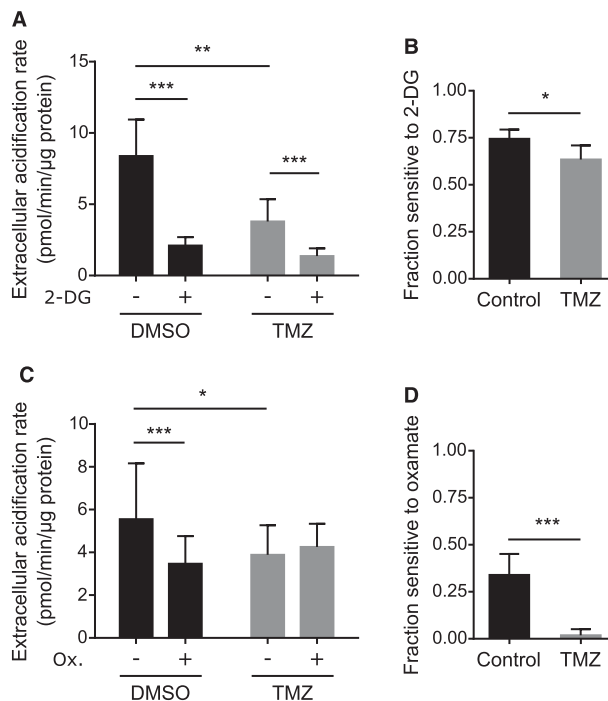


**Figure 3. Reduction in glucose catabolism to lactate in TMZ-induced senescence.**

The ECAR was evaluated before and after the addition of (A) 2-deoxyglucose (2-DG) or (C) oxamate. (B and D) The fraction of basal extracellular acidification sensitive to 2-DG (B) or oxamate (D), respectively, was calculated as described in the Experimental section ( $n = 10$  wells per group). Results are the mean  $\pm$  S.D. *T*-tests were performed, \*  $P < 0.05$ , \*\*  $P < 0.001$ , \*\*\*  $P < 0.0001$ .

but had practically no effect in that of senescent cells (Figure 3C,D). Overall, our results suggest that although glucose catabolism is a prominent pathway in both conditions, the conversion of pyruvate to lactate only occurs in control cells, while in senescent cells it is substituted by mitochondrial catabolic pathways.

## TMZ-induced senescent cells present increased mitochondrial content and biogenesis

To better understand the alterations in mitochondrial function that accompany the induction of senescence in melanoma cells, we used MitoTracker Green FM, a fluorescent probe that accumulates in mitochondria of living cells regardless of mitochondrial membrane potential. We performed flow cytometry assays and observed that senescent cells exhibited an increase in fluorescence intensity relative to control cells (Figure 4A), indicative of an increase in mitochondrial content per cell.

To confirm the increase in mitochondrial content in senescent cells, we measured the mtDNA/nDNA ratio [64] and the activity of citrate synthase per  $10^6$  cells, a constitutive enzyme present in the mitochondrial matrix [65]. A threefold increase in both parameters could be appreciated in senescent cells with respect to control cells (Figure 4B,C). However, when citrate synthase activity was normalized by total cell protein content (mg), no differences were observed between the two conditions (control  $0.17 \pm 0.01$  U/mg versus TMZ  $0.15 \pm 0.01$  U/mg,  $n = 3$ ), implying that the increase in mitochondrial mass accompanies the overall increase in cell protein mass. Similar results were obtained when equal quantities of cell proteins were resolved and blots performed with antibodies against subunits of the respiratory complexes: No differences were observed in protein levels relative to tubulin levels for most mitochondrial proteins (Supplementary Fig. S2B,C), confirming that the increase in mitochondrial mass encompasses the overall increase in mass of senescent cells. An exception was found for subunit II of complex IV, which is coded by mtDNA and presented a decrease in protein levels (Supplementary Fig. S2B,C).

We also looked into the proliferator-activated receptor gamma co-activator-1 (PGC-1) family, which is known to play a relevant role in the transcriptional control of mitochondrial biogenesis and respiratory function [66,67]. The increase in mitochondrial mass and mtDNA/nDNA ratio in senescent cells was accompanied by a twofold increase in PGC-1 $\alpha$  mRNA (Figure 4D) and a significant rise in mitochondrial transcription factor A (TFAM) levels (Figure 4E,F), while PGC-1 $\beta$  mRNA remained unchanged (control cells  $1.0 \pm 0.3$  versus TMZ cells  $1.1 \pm 0.3$ ,  $n = 3$ ). These observations suggest that TMZ-induced senescence in melanoma might be accompanied by an activation of mitochondrial biogenesis.

## TMZ-induced senescent cells present increased mitochondrial length

We then assessed mitochondrial morphology, by confocal microscopy, in cells stained with MitoTracker Green FM. Analysis of the images revealed that control cells presented mostly short rounded mitochondria, while elongated and more tubular mitochondria accumulated in senescent melanoma cells, and an increase in mitochondrial length could be determined by measuring mitochondria located in the periphery of the cell (Figure 4G). Frequency distribution analysis of mitochondrial length revealed that smaller mitochondria ( $<0.5 \mu\text{m}$ ) were more abundant in control cells with respect to senescent cells. While long mitochondria ( $>4.5 \mu\text{m}$ ) were mostly found in treated cells (Figure 4H), the Chi-square test for distribution analysis indicated significant differences ( $P < 0.0001$ ) between the two groups. Analysis of images obtained by transmission electron microscopy confirmed the increase in length of mitochondria from senescent cells with respect to control cells (Figure 4I).

## Alterations in mitochondrial fusion in TMZ-induced senescence

To better characterize the molecular events behind mitochondrial elongation in senescent cells, we analyzed the proteins involved in mitochondrial fusion and fission. A significant increment in mRNA and protein level of fusion proteins MFN1 and MFN2 was observed in senescent cells (Figure 5A–C). No differences were observed in fission proteins, OPA1 and DRP1; however, a significant decrease in FIS1 and in MFF was detected in TMZ-treated cells with respect to control cells (Figure 5A,B). Of note, western blot with the antibody against MFF revealed the presence of several bands with molecular mass between 25 and 35 kDa; in agreement with previous reports by others that show that MFF presents several isoforms and posttranslational modifications [68–72]. The decrease in FIS1 and MFF protein levels was not accompanied by a decrease in mRNA (Figure 5C).

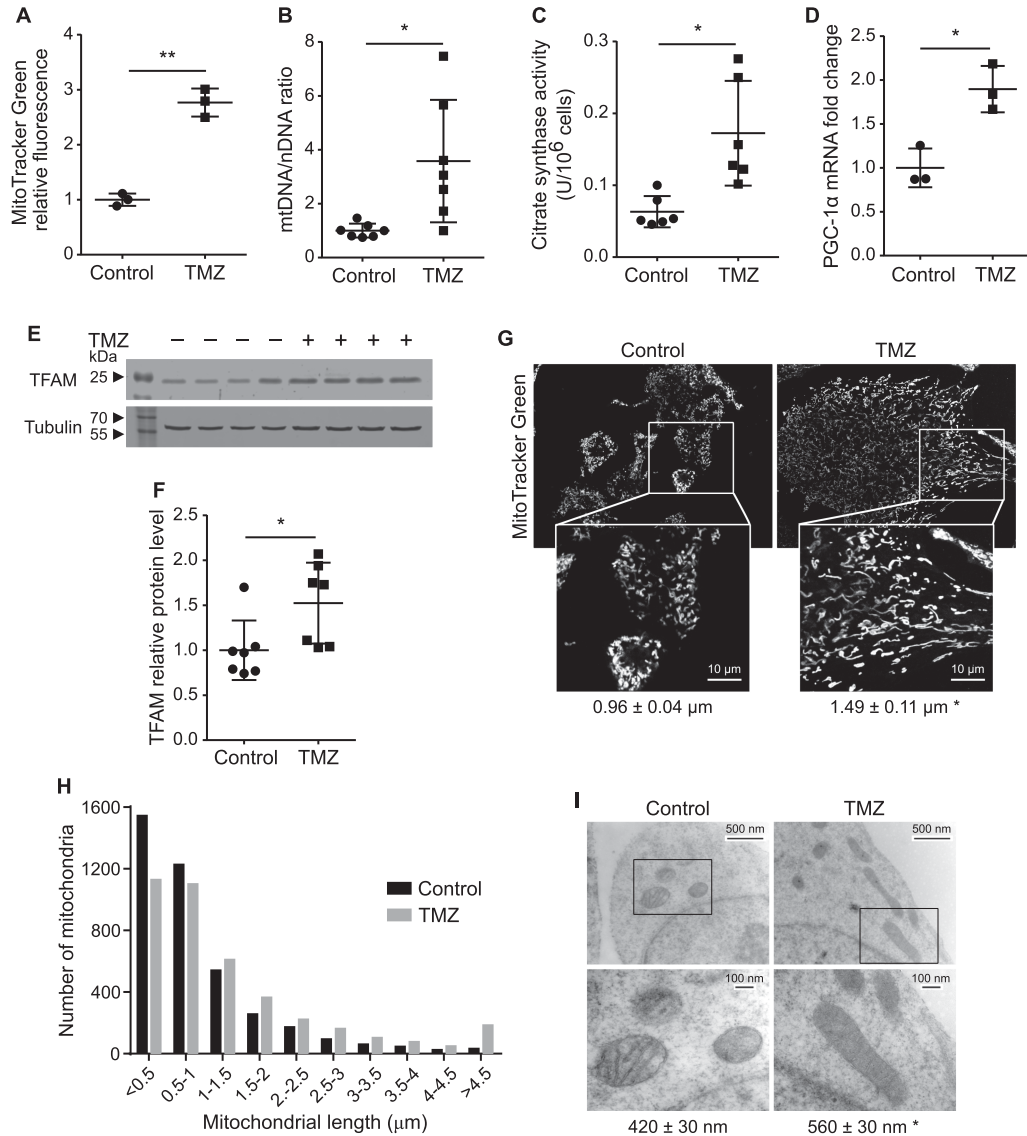


**Figure 4. TMZ-induced senescent cells present increased mitochondrial content and length.**

(A) Cells were stained with the mitochondrial fluorescent probe MitoTracker Green FM and mitochondrial mass was determined by flow cytometry. Geometrical mean fluorescence intensity of the cell population, relative to control values is shown ( $n = 3$  culture dishes per group). (B) MtDNA/nDNA ratio was assessed by real-time PCR. Results are expressed relative to the control condition ( $n = 7$  culture dishes per group). (C) Citrate synthase activity was measured and normalized by  $10^6$  cells ( $n = 6$  culture dishes per group). (D) Real-time RT-PCR was performed for PGC-1 $\alpha$  expression. Results are expressed relative to the control condition ( $n = 3$  culture dishes per group). (E) Representative western blots were performed with antibodies for TFAM and tubulin. (F) TFAM protein levels were quantified, from E, and normalized using tubulin as loading control ( $n = 7$  culture dishes per group). Results are expressed relative to control condition. (G) Representative images of living cells stained with MitoTracker Green FM and analyzed by the confocal microscopy ( $\times 630$ ) ( $n = 6$  slides per condition were assessed). Magnified images of the boxed regions are shown below. Average mitochondrial length is shown below the pictures ( $n = 6$  slides per group). (H) Frequency distribution analysis of mitochondrial length from images like those presented in (G). Statistical analysis included contingency tables and a Chi-square test ( $P < 0.0001$ ). (I) Representative electron transmission microscopy images obtained at  $\times 20\,000$  (top) and  $\times 50\,000$  (bottom). The bottom images are the magnified images of the boxed region. Average mitochondrial length is shown below the pictures ( $n = 3$  culture dishes per condition). Results are the mean  $\pm$  S.D. *T*-tests were performed, \*  $P < 0.05$ , \*\*  $P < 0.001$ .

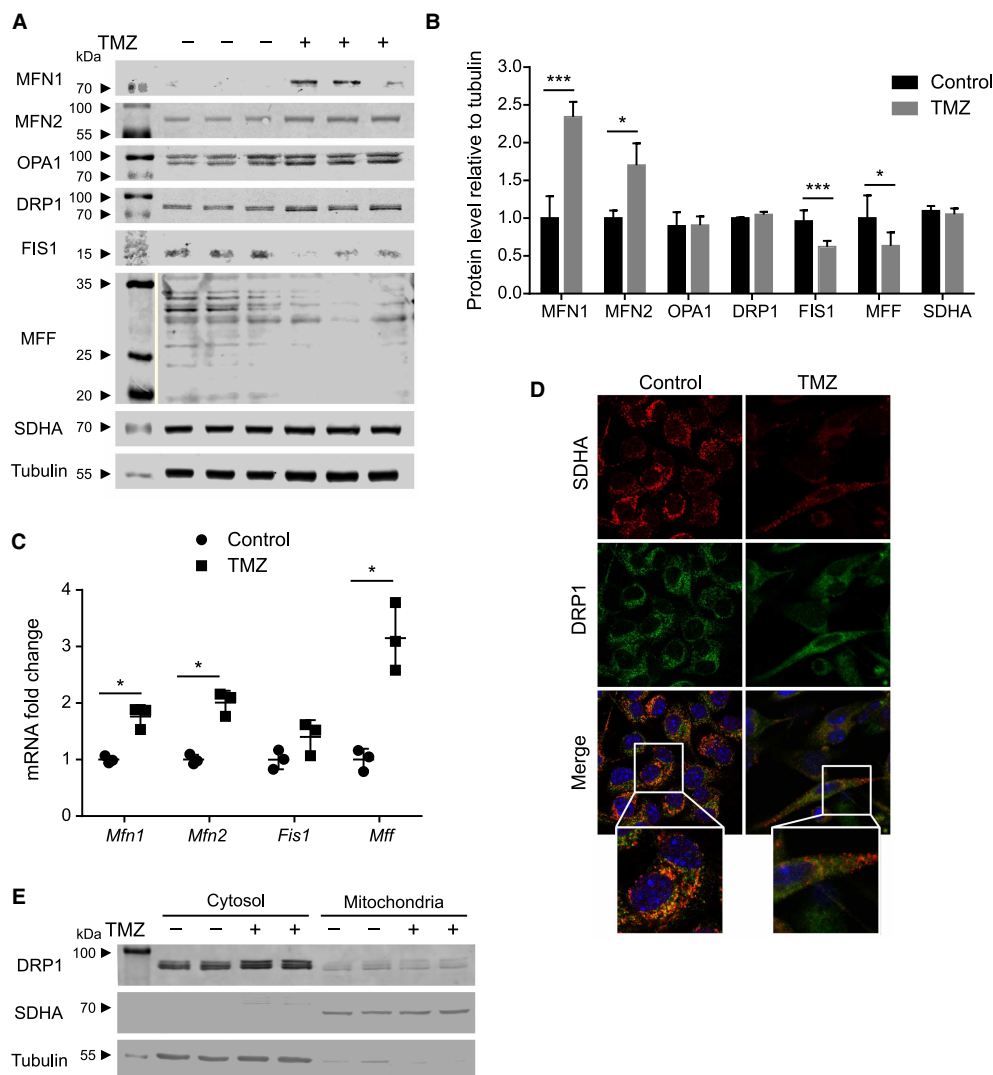


**Figure 5. Increase in mitochondrial fusion in TMZ-induced senescence.**

(A) Representative western blots for mitochondrial fusion and fission proteins MFN1, MFN2, OPA1, DRP1, FIS1, MFF, SDHA and tubulin as loading control ( $n = 3$  culture dishes per group). (B) Protein levels in independent western blots were quantified by densitometry and normalized using tubulin as loading control. Results are expressed relative to control condition ( $n = 3$ –10 culture dishes per group). (C) Real-time RT-PCR was performed for *Mfn1*, *Mfn2*, *Fis1* and *Mff*. Results are expressed relative to the control condition ( $n = 3$  culture dishes per group). (D) Representative images of colocalization of SDHA (red) and DRP1 (green). DAPI (blue) were used to stain the nuclei. Pearson correlation coefficients were  $0.40 \pm 0.02$  for control, and  $0.34 \pm 0.02$  for TMZ ( $P < 0.05$ ,  $n = 4$  coverslips per group). Enhanced images of the boxed regions (gray rectangle) are shown in the lower panel. (E) Representative western blot for DRP1, SDHA and tubulin in subcellular fractions enriched in mitochondria or cytosol. Results are the mean  $\pm$  S.D. *T*-tests were performed, \*  $P < 0.05$ , \*\*\*  $P < 0.0001$ .

Mitochondrial fission requires the recruitment of DRP1 to the outer mitochondrial membrane and MFF is considered the principal recruitment factor [70,73,74]. Thus, we assessed if the translocation of DRP1 to the mitochondria was affected. DRP1 colocalization with subunit A of the mitochondrial protein succinate dehydrogenase (SDHA) was slightly lower in senescent than non-senescent cells (Pearson correlation coefficients for control  $0.40 \pm 0.02$  and TMZ  $0.34 \pm 0.02$ ,  $P < 0.05$ ) (Figure 5D). However, subcellular fractionation did not show significant differences in DRP1 content in mitochondria from treated and untreated cells (Figure 5E).

Altogether, these results suggest that the increase in mitochondrial length, observed in senescent cells, is due to an increase in fusion events mediated by MFN 1 and 2.

## Alterations in mitochondrial function are specifically associated to the induction of senescence

Since exposure to TMZ leads to the appearance of senescent markers in many but not all of the cells in the culture (Figure 1), and because electron transport chain activity is increased in TMZ resistance in glioma cells [75], we wondered if the increase in mitochondrial function was linked specifically to the induction of senescence or mainly a consequence of TMZ treatment.

We took advantage of the difference in cell size and granularity between senescent and non-senescent cells to sort TMZ-treated cells into two populations. Following the same criteria as in Figure 1F, cells were separated in two groups: large and more granular cells (TMZ (Large)) and smaller and less granular cells (TMZ (Small)) (Figure 6A). Control cells were mainly small and with low granularity and very few large complex cells could be found in the culture. Measurement of SA- $\beta$ -gal activity confirmed the enrichment of senescent cells in TMZ (Large) population compared with TMZ (Small) (Figure 6B). The analysis of mitochondrial OCR showed that TMZ (Large) cells had substantially higher basal, ATP-dependent, maximum and non-mitochondrial respiration rates (Figure 6C) than control and TMZ (Small) cells. They also had higher coupling efficiency, spare capacity, and RCRs (Table 2). Therefore, senescent cells were the main population responsible for the increase in mitochondrial OCR observed after treatment with TMZ. Nevertheless, a small but significant increase in coupling efficiency could be found in TMZ-treated non-senescent cells (TMZ (Small)) when compared with control cells (Table 2), which requires further exploration.

Confocal evaluation of sorted cells stained with MitoTracker Green FM showed that mean mitochondrial length was significantly higher in TMZ (Large) cells than in control cells (TMZ (Large)  $1.8 \pm 0.2 \mu\text{m}$  versus control  $0.97 \pm 0.09 \mu\text{m}$ ,  $n = 3-6$ ,  $P < 0.0001$ ) and TMZ (Small) cells (Figure 6D). Frequency distribution analysis of mitochondrial length showed that short mitochondria ( $<0.5 \mu\text{m}$ ) were clearly more abundant in control than in TMZ-treated cells (both Large and Small). While long mitochondria ( $>4.5 \mu\text{m}$ ) were mostly found in TMZ (Large) cells (Figure 6E), they could be considered as a characteristic of senescent cells. Similar results were obtained for mitochondrial mass, which was also higher in TMZ (Large) cells than TMZ (Small) cells (TMZ (Large)  $1.00 \pm 0.06$  versus TMZ (Small)  $0.27 \pm 0.05$ ,  $n = 3$ ,  $P < 0.0001$ ).

Evaluation of mitofusin expression in sorted cells revealed that mRNA levels of MFN1 and 2 of TMZ (Large) cells were significantly higher than those of control cells (MFN1: control  $1 \pm 0.1$  versus TMZ (Large)  $2.0 \pm 0.7$ ,  $n = 6-7$ ,  $P < 0.01$ ; MFN2: control  $1 \pm 0.1$  versus TMZ (Large)  $2.1 \pm 0.8$ ,  $n = 6-7$ ,  $P < 0.05$ ). But, no significant differences were found between TMZ (Small) and control cells. In sum, our results point towards mitochondrial changes in size, mass and function being characteristics of senescent cells.

## Silencing of *Mfn1* and 2 impacts on the SASP

To further understand whether the observed changes in mitochondrial morphology and function contributed to the phenotype of senescent cells, we transduced melanoma cells with lentiviral particles carrying shRNA targeting *Mfn1* or *Mfn2*, or scrambled shRNA (Scr), and selected with puromycin, prior to the treatment with either DMSO or TMZ.

Stable genetic inhibition of *Mfn2* (Figure 7A–C) did not significantly reduce the average mitochondrial length of DMSO or TMZ-treated cells (Supplementary Fig. S3A). However, frequency distribution of the population revealed that *Mfn2* silencing resulted in an increase in small mitochondria ( $<0.5 \mu\text{m}$ ) with respect to control (Scr) cells and precluded the formation of long mitochondria ( $>4.5 \mu\text{m}$ ) in response to treatment with TMZ (Figure 7D,E). Significant differences were found between the distributions upon Chi-square test analysis ( $P < 0.0001$ ).

Targeting of *Mfn2* did not affect mitochondrial respiratory parameters of cells treated with vehicle; but resulted in a decrease in basal, ATP-dependent and maximum respiration of TMZ-treated cells (Figure 7F). These results suggest mitochondrial fusion might be involved in the increase in mitochondrial bioenergetics, observed in senescent cells. Flow cytometry analysis of MitoTracker Green FM fluorescence showed that after exposure to TMZ, the increase in mitochondrial mass was 30% higher in cells where *Mfn2* was silenced than in those where it was not (Scr) (Supplementary Fig. S3B). These results further support that *Mfn2* silencing

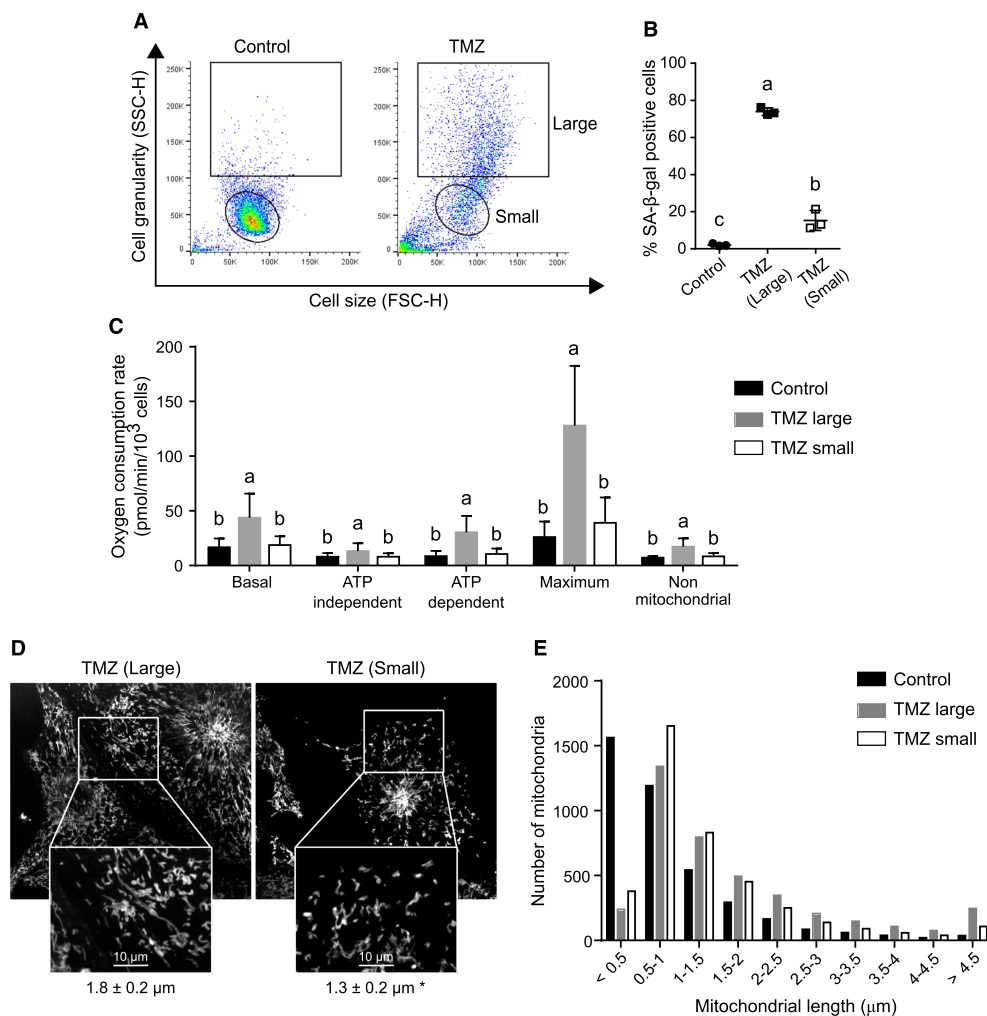


**Figure 6. Isolation of senescent cells by cell sorting and analysis of mitochondrial function and dynamics.**

TMZ-treated cells were separated by cell sorting. (A) Representative dot plots show the regions selected to separate two populations of TMZ-treated cells: larger and granular senescent cells (Large) from smaller and less granular non-senescent cells (Small). The gating for selection of small and large cells was set up using the corresponding control and TMZ-treated cultures. (B) Quantification of SA-β-gal activity assay assessed after cell sorting ( $n = 3$  culture dishes per condition). (C) Respiratory parameters were obtained, as described in Figure 2 ( $n = 18$ – $21$  wells per group). (D) Living cells were stained with the MitoTracker Green FM and analyzed by confocal microscopy ( $\times 630$ ). Representative images and magnified images of the boxed regions (white rectangle) are shown. Average mitochondrial length is shown below the pictures ( $n = 3$ – $6$  slides per group). (E) Frequency distribution analysis of mitochondrial length from samples in (D). Statistical analysis included contingency tables and a Chi-square test ( $P < 0.0001$ ). Results are the mean  $\pm$  S.D. One-way ANOVA and Tukey post hoc tests were performed; groups with different letters or an asterisk are significantly different ( $P < 0.05$ ).

impacts negatively on mitochondrial function, since it inhibits respiration in spite of the increase in mitochondrial mass.

We then explored if *Mfn2* silencing affected the induction of senescence. Our results show that decreased levels of *Mfn2* did not reduce the percentage of SA-β-gal positive cells (Figure 7G); or affect proliferation arrest in the TMZ-treated culture (Supplementary Fig. S3C); yet resulted in a significant inhibition of interleukin 6 (IL-6) secretion by TMZ-treated cells, without affecting the DMSO-treated culture (Figure 7H).

Similar results were obtained after inhibition of *Mfn1* expression (Figure 8A,B). Average mitochondrial length of cells treated with DMSO or TMZ was not affected by *Mfn1* silencing (Supplementary Fig. S3D). Yet, analysis of the frequency distribution revealed an important increase in small mitochondria ( $< 1 \mu\text{m}$ ) in

**Table 2 Mitochondrial respiratory ratios of senescent cells separated by cell sorting**

Respiratory ratios	Control	TMZ (Large)	TMZ (Small)
Coupling efficiency	0.49 ± 0.06 <sup>c</sup>	0.71 ± 0.05 <sup>a</sup>	0.56 ± 0.03 <sup>b</sup>
Spare respiratory capacity	1.5 ± 0.2 <sup>b</sup>	3.2 ± 1.0 <sup>a</sup>	1.9 ± 0.5 <sup>b</sup>
Respiratory control ratio	3.0 ± 0.6 <sup>b</sup>	12 ± 6 <sup>a</sup>	4 ± 1 <sup>b</sup>

Coupling efficiency, spare respiratory capacity and respiratory control rate were calculated from OCR measurements in Figure 6C. Results are the mean ± S.D. (*n* = 18–21 wells per group). One-way ANOVA showed significant differences between groups for the three respiratory ratios (*P* < 0.0001). For multiple comparisons Tukey post-hoc tests were performed, groups with different letters (a, b or c) are significantly different from each other (*P* < 0.0001) in all cases.

untreated cells where *Mfn1* had been silenced, with respect to control (Scr) cells. Besides the decrease in MFN1 levels prevented the formation of long mitochondria (>4.5 μm) upon treatment with TMZ (Figure 8C,D) and significant differences between distributions could be found by the Chi-square test analysis (*P* < 0.0001).

Surprisingly, the decrease in MFN1 levels did not significantly affect mitochondrial respiration of DMSO or TMZ-treated cells (Supplementary Fig. S3E). Flow cytometry analysis of MitoTracker Green FM fluorescence showed that after exposure to TMZ, the increase in mitochondrial mass was 50% higher in cells where *Mfn1* was silenced than in those where it was not (Scr) (Supplementary Fig. S3F), and might explain the absence of changes on mitochondrial OCRs. Nevertheless, assessment of markers of senescence revealed that the decrease in MFN1 levels reduced the percentage of SA-β-gal positive cells and the secretion of IL-6 in the TMZ-treated culture without affecting non-treated cells (Figure 8E,F).

To check for off-target effects, a second shRNA was used to silence *Mfn1* expression. Similar results were obtained with this construct, which resulted in a decrease in mitochondrial length and in IL-6 secretion in TMZ-treated cells; while OCRs remained unchanged (Supplementary Fig. S4).

Altogether these results suggest that mitofusins mediate the increase in mitochondrial length and size; and appear to be required for acquisition of the senescent-associated secretory phenotype in TMZ-induced senescence in melanoma cells.

## Discussion

This work focused in the study of energy metabolism of senescent cells in a model of therapy-induced senescence in melanoma. With this aim, we induced senescence in mouse melanoma cells by exposure to the genotoxic TMZ. About 60–70% of the culture became senescent after treatment and acquired a SASP composed of cytokines and growth factors. Induction of senescence was dependent on the activation of the p53/p21 pathway; in agreement with previous reports [11].

Senescent cells underwent important bioenergetic alterations. While melanoma B16-F1 cells presented a highly glycolytic energy metabolism, where glucose was converted to lactate, senescent cells had reduced lactate formation and increased mitochondrial function. In senescent cells, respiration was augmented, electron transport was better coupled to ATP synthesis and mitochondria were more prepared to face increases in energy demands. The increase in mitochondrial respiration rates surpassed the changes in cell mass. Thus, induction of senescence resulted in a reversal of the Warburg effect and activation of oxidative phosphorylation, in consonance with the decrease in proliferation [76–78].

Although mitochondrial dysfunction has been observed in certain models of senescence [30–32], and can *per se* induce senescence [79], it is not a characteristic of senescent cells. In fact, our results show that in melanoma cells undergoing TMZ-induced senescence, mitochondria are not dysfunctional, on the contrary they present high activity, evidenced by the increase in respiration rates and indexes, such as coupling efficiency, spare respiratory capacity and RCR. Moreover, a similar increase in mitochondrial function was observed in oncogene-induced senescent cells [27].

The increment in mitochondrial mass could account for part of the alterations in mitochondrial respiration observed in senescent melanoma cells. Increased expressions of PGC-1α and TFAM were observed upon induction of senescence. PGC-1α promotes the expression of several proteins involved in respiration and of TFAM, a

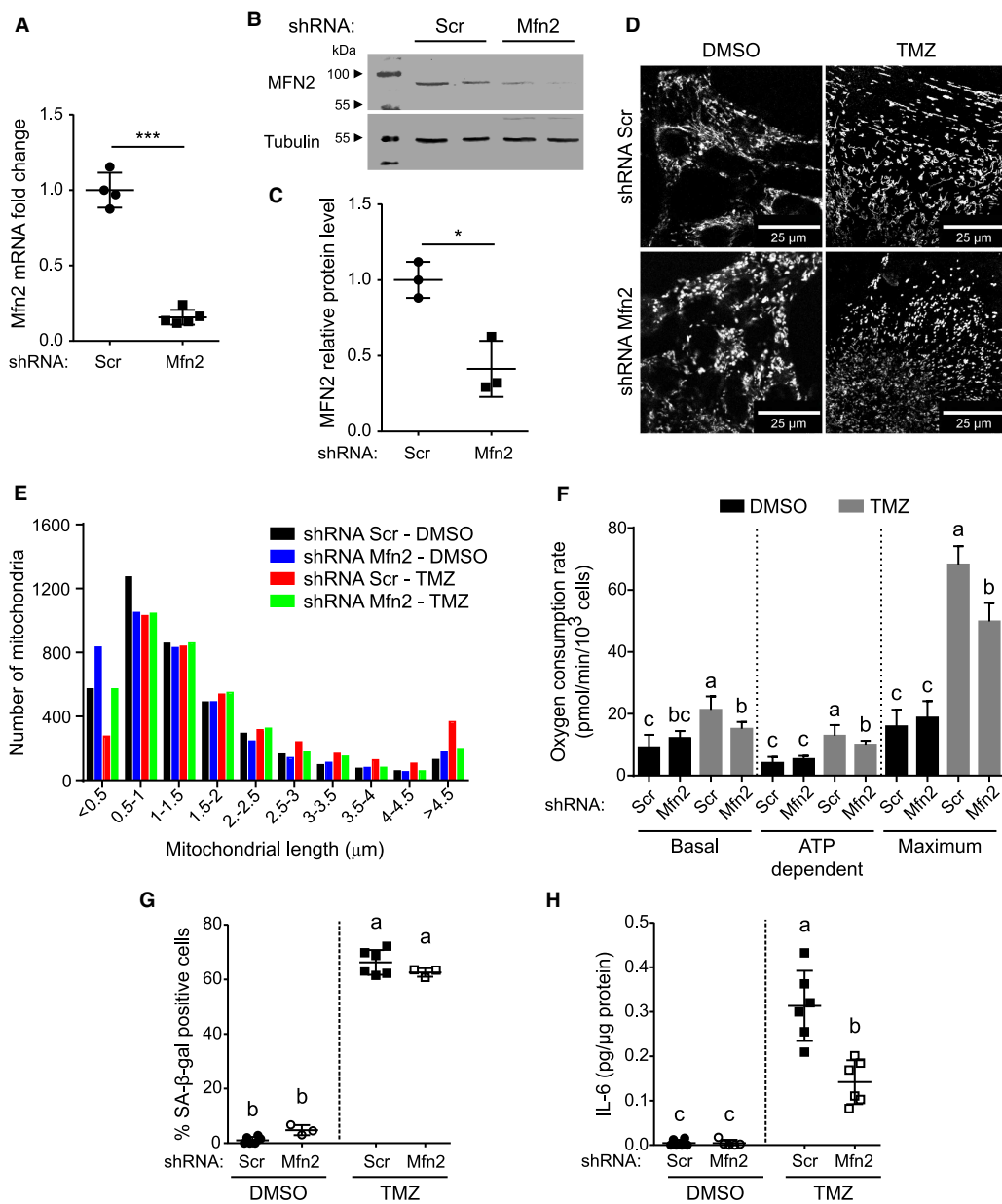


**Figure 7. Mitofusin 2 silencing affects mitochondrial size and function and reduces IL-6 secretion in TMZ-induced senescence cells.**

Part 1 of 2

Melanoma cells were transduced with lentiviral particles carrying short hairpin (shRNA) targeting *Mfn2*, or scrambled shRNA (Scr), and selected with puromycin, prior to treatment with DMSO or TMZ. **(A)** Real-time RT-PCR for *Mfn2* ( $n = 4-5$  culture dishes per group). Results were expressed relative to the condition Scr - DMSO. **(B)** Representative western blots for MFN2 and tubulin. **(C)** Quantification of protein levels in western blots is shown in **(B)**. MFN2 was normalized using tubulin as loading control and results were expressed relative to control condition (Scr) ( $n = 3$  culture dishes per group). **(D)** Representative images of living cells stained with MitoTracker Green FM and analyzed by confocal microscopy ( $\times 630$ ). **(E)** Frequency distribution analysis of mitochondrial length from samples like those shown in **(D)**. Statistical analysis included contingency tables and a Chi-square test ( $P < 0.0001$ ). **(F)** Respiratory parameters obtained as described in **Figure 2** ( $n = 5-10$  wells per group). Main effects of treatment, shRNA and their interaction respectively for: basal OCR ( $P < 0.0001$ ,  $P = 0.24$ ,  $P < 0.05$ ); ATP dependent OCR ( $P < 0.0001$ ,  $P = 0.36$ ,  $P < 0.05$ ); maximum OCR ( $P < 0.0001$ ,  $P < 0.05$ ,  $P < 0.0001$ ). **(G)** Quantification of SA- $\beta$ -gal positive cells ( $n = 3-6$  wells per group). Main effects of treatment ( $P < 0.0001$ ), shRNA ( $P = 0.99$ ) and interaction ( $P < 0.05$ ). **(H)** IL-6 secretion levels were analyzed by ELISA ( $n = 5-6$  wells per group). Main effects of treatment ( $P < 0.0001$ ), shRNA ( $P < 0.001$ ) and interaction ( $P < 0.001$ ). *T*-tests were performed in **(A)** and **(C)** \*  $P < 0.05$ , \*\*\*  $P < 0.0001$ . Statistical significance of main effects of

**Figure 7. Mitofusin 2 silencing affects mitochondrial size and function and reduces IL-6 secretion in TMZ-induced senescence cells.**

Part 2 of 2

treatment, shRNA and their interaction, were determined by two-way ANOVA, and Tukey post hoc for multiple comparisons in figures F–H; groups with different letters are significantly different ( $P < 0.05$ ). In all graphs results are the mean  $\pm$  S.D.

direct regulator of mitochondrial DNA replication and transcription [66,67]. Besides, PGC-1 $\alpha$  is known to promote mitochondrial biogenesis in several physiological settings including cancer [35,80] and might be behind the increase in mitochondrial mass in our model. Changes in mitophagy might play a role as well, but were not investigated in this opportunity. Interestingly, FIS1, which has been implied in the coupling of mitochondrial fission and mitophagy [81], had lower protein levels in senescent than non-senescent cells. Although an increase in mtDNA was observed in senescent cells, a decrease in protein levels of subunit II of Complex IV was observed, which might be due to increased degradation [82]. Subunit II forms part of the functional core of the complex that catalyzes the reduction in oxygen to water [83], yet its decrease did not prevent senescent cells from presenting high respiration rates. These results are in agreement with reports showing that the activity of Complex IV exceeds what is required to sustain respiration, and might not be the limiting step controlling respiration rate [84,85].

In addition to an increase in mass, an increase in mitochondrial length accompanied the induction of senescence, and was associated with an increase in fusion proteins MFN1 and 2. Although a decrease in fission-related proteins MFF and FIS1 could be observed after treatment, the translocation of DRP1 to mitochondria remained practically unchanged. Suggesting an increase in fusion events, mediated by an increase in mitofusins levels, as the main responsible of changes in mitochondrial length. PGC-1 $\alpha$  can regulate *Mfn2* gene expression [86], and might play a role in this setting. Longer and more interconnected mitochondria have been reported to present higher levels of oxidative phosphorylation than small, fragmented mitochondria [31,87–90]. Yet the relation between mitochondrial morphology and function is complex, and similar alterations in morphology (e.g. fragmentation or filamentation) can have different outcomes depending on the cell type and physiological context. [38,91,92].

An increase in mitochondrial length, due to changes in fusion and fission, had also been observed in senescence induced by desferrioxamine and hydrogen peroxide in fibroblasts [93], although mitochondrial respiration was not measured and the mtDNA/nDNA ratio decreased in this model. Besides, an interesting report showed that FIS1 depletion increased mitochondrial length and ROS-mediated activation of the DNA damage response, leading to the induction of senescence [94] in Chang cells.

Increased levels of proteins involved in oxidative phosphorylation and respiration [34] can also be found in slow-cycling melanoma cells that are highly resistant to cytotoxic therapies. These reports raised the possibility that the increase in mitochondrial function was linked to the decrease in proliferation rates. However, quiescent fibroblasts, with a reversible arrest in proliferation [95], present lower and more uncoupled mitochondrial respiration rates than their proliferating counterparts; along with increased fragmentation of the mitochondrial network and lower levels of MFN1 and 2 [90]. Decreased mitochondrial potential and mass were reported in quiescent glioblastoma cells from tumor spheroids [96]; and mitochondrial fragmentation and a donut phenotype was observed in quiescent glioblastoma stem-like cells [97]. Thus, although an increased mitochondrial function might be a common characteristic of cells surviving treatment with genotoxic agents, it does not appear to be linked to proliferation arrest *per se*.

To investigate if the changes in mitochondrial shape and function played a role in senescence, we silenced *Mfn1* and *Mfn2* expression. The decrease in mitofusin levels prevented the formation of long mitochondria in TMZ-treated cultures, and in the case of MFN2 also impacted respiration rates of treated cells. Silencing of either *Mfn1* or *Mfn2* inhibited the secretion of the proinflammatory cytokine IL-6 in TMZ-induced senescent cells, and a reduction in the percentage of senescent cells in the culture was also observed. Altogether, our observations support that the increase in mitochondrial fusion versus fission processes might be responsible for the increase in electron transport chain activity and appears to play a role maintaining the senescent phenotype, in particular the SASP. However, the fact that in cells with low MFN1 IL-6 secretion was affected, but not OCRs, indicates that lack of ATP might not be the event behind the inhibition of interleukin synthesis and secretion. MFN2 modulates the association between mitochondria to the endoplasmic reticulum, where IL-6 and other components of the SASP are synthesized [98]. Besides, it has been reported to participate in NLRP3 inflammasome activation and secretion of IL-1 $\beta$  in macrophages [99] and the inflammasome is known to

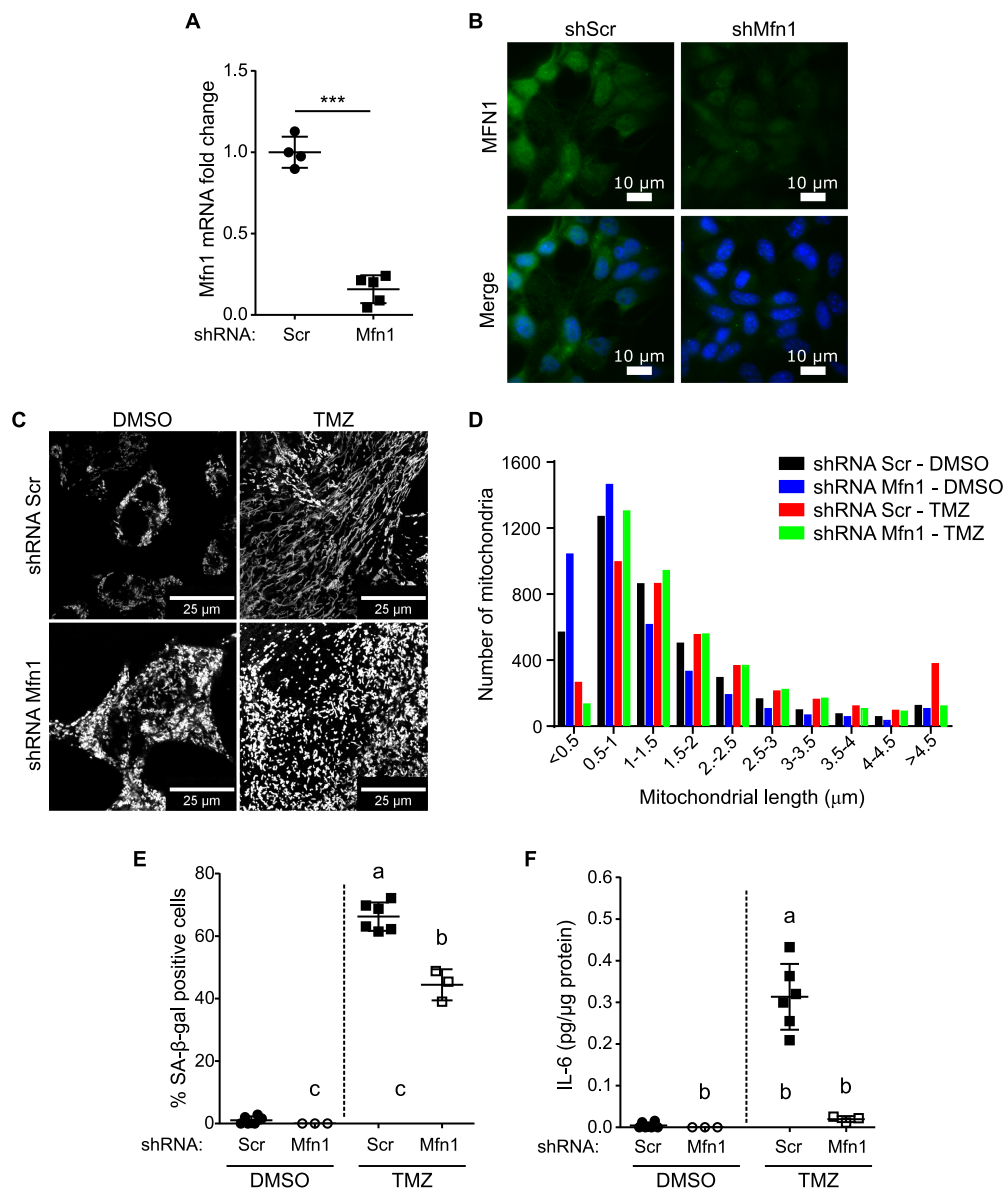


**Figure 8. Mitofusin 1 silencing affects mitochondrial size and reduces IL-6 secretion of TMZ-induced senescence cells.**

Melanoma cells were transduced with lentiviral particles carrying short hairpin (shRNA) targeting *Mfn1*, or scrambled shRNA (Scr), and selected with puromycin, prior to the treatment with either DMSO or TMZ. **(A)** Real-time RT-PCR for *Mfn1* ( $n = 4-5$  culture dishes per group). Results were expressed relative to the condition Scr - DMSO. **(B)** Representative images of MFN1 staining with an anti-MFN1 antibody (green) and DAPI (blue) to stain the nuclei, obtained by immunocytochemistry and epifluorescence microscopy ( $\times 1000$ ). **(C)** Living cells were stained with MitoTracker Green FM and analyzed by confocal microscopy ( $\times 630$ ). **(D)** Frequency distribution analysis of mitochondrial length from samples in **(C)**. Statistical analysis included contingency tables and a Chi-square test ( $P < 0.0001$ ). **(E)** Quantification of SA- $\beta$ -gal positive cells ( $n = 3-6$  wells per group). Main effects of treatment ( $P < 0.0001$ ), shRNA ( $P < 0.0001$ ) and interaction ( $P < 0.0001$ ). **(F)** IL-6 secretion was analyzed by ELISA ( $n = 3-6$  wells per group). Main effects of treatment ( $P < 0.0001$ ), shRNA ( $P < 0.0001$ ) and interaction ( $P < 0.0001$ ). *T*-test was performed in **(A)**  $*** P < 0.0001$ . Statistical significance of main effects of treatment, shRNA and their interaction, were determined by two-way ANOVA, and Tukey post hoc for multiple comparisons (**E** and **F**), groups with different letters are significantly different ( $P < 0.05$ ). Results are the mean  $\pm$  S.D.

control the SASP in oncogene-induced senescence [100]. We aim to explore these pathways in therapy-induced senescence, in future investigations to further understand the mechanisms behind mitofusin regulation of the secretome.

Senescence is one of the outcomes of chemotherapy, radiotherapy and targeted therapies in melanoma [10,12,20,23]; and through proliferation arrest or the SASP can exert effects on cancer progression. The senescent secretome can affect tumor cell proliferation and migration, the immune response to the tumor, the extracellular matrix and angiogenesis [17,18]. However, the detrimental or benefic effects of the SASP in cancer depend on the cell type undergoing senescence, the senescence inducer, the tissue where the secreted factors exert their effect and the timing [17,18,101]. Conflicting results can be found in melanoma, where CCL2 and IL-6 secreted by therapy-induced senescent cells promote tumor formation, invasiveness and resistance to apoptosis [8,21]. But, CCL5 formed during therapy-induced senescence recruit leukocytes inhibiting melanoma tumor growth [23]. Thus, further research is required to establish the positive or negative effects of therapy-induced senescence in melanoma.

Although the impact of senescent cells arising during chemotherapy on tumor progression is not completely elucidated, pharmacological approaches targeting senescent cells and the SASP are being explored. These have led to the development of senolytics, drugs that promote selective death of senescent cells [17,102]; as well as senomorphics, drugs that reduce the SASP without inducing cell death [101]. Reports show synergy between senolytics and chemotherapeutics killing cancer cells [19,103]. Results presented herein, along with previous reports showing that inhibition of mitochondrial energy metabolism decreases the secretion of proinflammatory cytokines [27,104], indicate that mitochondria constitute an appealing pharmacologic target to modulate the SASP.

Our results provide an in-depth assessment of mitochondrial function in senescent cells, and identify mitochondrial fusion proteins, mitofusins, as plausible pharmacological targets to modulate the SASP. These results contribute to understand metabolic adaptations in therapy-induced senescence and provide insight for the design of senolytics and senomorphics targeting mitochondrial energy metabolism and dynamics. However, further studies are required to provide mechanistic insights both on the regulation of mitofusin expression in senescence; and their role in the synthesis and secretion of IL-6 and other components of the SASP.

### Abbreviations

2-DG, 2-deoxyglucose; AA, antimycin A; ATM, ataxia-telangiectasia mutated kinase; BCA, bichinchoninic acid; Brdu, bromodeoxyuridine; CB, cacodylate buffer; DAPI, 4',6-diamidino-2-phenylindole; DMEM, Dulbecco's modified Eagle's medium; DMSO, dimethyl sulfoxide; DRP1, dynamin-related protein 1; ECAR, extracellular acidification rate; FCCP, carbonyl cyanide 4-(trifluoromethoxy)phenylhydrazone; FIS1, mitochondrial fission 1 protein; IL-6, interleukin 6; MFF, mitochondrial fission factor; MFN1, mitofusin 1; MFN2, mitofusin 2; OCR, oxygen consumption rate; OPA1, optic atrophy protein 1 homolog; p16-INK4, cyclin-dependent kinase inhibitor 2A; p21, cyclin-dependent kinase inhibitor 1; PGC-1, proliferator-activated receptor gamma co-activator-1; pRb, retinoblastoma protein; RCR, respiratory control ratio; ROS, reactive oxygen species; SASP, senescence-associated secretory phenotype; SA- $\beta$ -gal, senescence associated  $\beta$ -galactosidase; Scr, scrambled shRNA; SDHA, succinate dehydrogenase subunit A; shRNA, short hairpin RNA; TFAM, mitochondrial transcription factor A; TMZ, temozolomide;  $\gamma$ -H2AX, phosphorylated histone H2AX.

### Author Contribution

C.Q., C.A. and J.M. conceived, designed and analyzed most of the experiments. M.M. designed the RT-qPCR primers and experiments. J.M. performed most of the experiments. D.T. obtained plasmids, prepared lentiviral particles and contributed to all experiments with shRNA. I.M. performed western blots and maintained tissue cultures. S.R.B., L.M.P. and P.C. contributed to obtain and analyze confocal microscopy images. G.C. obtained the transmission electron microscopy images. S.V. and M.B.F. performed and designed the cellular sorting, respectively. M.B. and C.E. measured IL-6 secretion. J.M. and C.Q. and wrote the manuscript. All authors reviewed the results and approved the final version of the manuscript.

### Funding

Agencia Nacional de Investigación e Innovación (ANII) FCE\_1\_2017\_1\_136021 and FCE\_2\_2011\_1\_6381 to C.Q.; Comisión Sectorial de Investigación Científica (CSIC) of the Universidad de la República (UdelaR) CSIC I+D 2012 ID47 and Roche Educational Grant to C.Q. and C.A.; CSIC UdelaR, Iniciación 2015 ID164; ANII

POS\_NAC\_2015\_1\_109506 and Comisión Académica de Posgrados (CAP) of the UdelaR to J.M.; Espacio Interdisciplinario Centros 2015, UdelaR; Programa de Desarrollo de las Ciencias Básicas (PEDECIBA).

## Acknowledgements

The authors thank Dr. Beatriz Alvarez, Dr. Toren Finkel and Dr. Adriana Cassina for their suggestions and comments on the manuscript; laboratory members for helpful discussions and Dr. Mercedes Rodríguez Teja for sequencing several plasmids.

## Competing Interests

The Authors declare that there are no competing interests associated with the manuscript.

## References

- 1 Campisi, J. (2013) Aging, cellular senescence, and cancer. *Annu. Rev. Physiol.* **75**, 685–705 <https://doi.org/10.1146/annurev-physiol-030212-183653>
- 2 Vredevelde, L.C., Possik, P.A., Smit, M.A., Meissl, K., Michaloglou, C., Horlings, H.M. et al. (2012) Abrogation of BRAFV600E-induced senescence by PI3K pathway activation contributes to melanomagenesis. *Genes Dev.* **26**, 1055–1069 <https://doi.org/10.1101/gad.187252.112>
- 3 Gray-Schopfer, V.C., Cheong, S.C., Chong, H., Chow, J., Moss, T., Abdel-Malek, Z.A. et al. (2006) Cellular senescence in naevi and immortalisation in melanoma: a role for p16? *Br. J. Cancer* **95**, 496–505 <https://doi.org/10.1038/sj.bjc.6603283>
- 4 Collado, M. and Serrano, M. (2010) Senescence in tumours: evidence from mice and humans. *Nat. Rev. Cancer* **10**, 51–57 <https://doi.org/10.1038/nrc2772>
- 5 Ewald, J.A., Desotelle, J.A., Wilding, G. and Jarrard, D.F. (2010) Therapy-induced senescence in cancer. *J. Natl Cancer Inst.* **102**, 1536–1546 <https://doi.org/10.1093/jnci/djq364>
- 6 Vance, K.W., Carreira, S., Brosch, G. and Goding, C.R. (2005) Tbx2 is overexpressed and plays an important role in maintaining proliferation and suppression of senescence in melanomas. *Cancer Res.* **65**, 2260–2268 <https://doi.org/10.1158/0008-5472.CAN-04-3045>
- 7 Giuliano, S., Cheli, Y., Ohanna, M., Bonet, C., Beuret, L., Bille, K. et al. (2010) Microphthalmia-associated transcription factor controls the DNA damage response and a lineage-specific senescence program in melanomas. *Cancer Res.* **70**, 3813–3822 <https://doi.org/10.1158/0008-5472.CAN-09-2913>
- 8 Ohanna, M., Giuliano, S., Bonet, C., Imbert, V., Hofman, V., Zangari, J. et al. (2011) Senescent cells develop a PARP-1 and nuclear factor- $\kappa$ B-associated secretome (PNAS). *Genes Dev.* **25**, 1245–1261 <https://doi.org/10.1101/gad.625811>
- 9 Baillet, O., Fenouille, N., Abbe, P., Robert, G., Rocchi, S., Gonthier, N. et al. (2009) Spleen tyrosine kinase functions as a tumor suppressor in melanoma cells by inducing senescence-like growth arrest. *Cancer Res.* **69**, 2748–2756 <https://doi.org/10.1158/0008-5472.CAN-08-2690>
- 10 Haferkamp, S., Borst, A., Adam, C., Becker, T.M., Motschenbacher, S., Windhövel, S. et al. (2013) Vemurafenib induces senescence features in melanoma cells. *J. Invest. Dermatol.* **133**, 1601–1609 <https://doi.org/10.1038/jid.2013.6>
- 11 Mhaidat, N., Zhang, X., Allen, J., Avery-Kiejda, K., Scott, R. and Hersey, P. (2007) Temozolomide induces senescence but not apoptosis in human melanoma cells. *Br. J. Cancer* **97**, 1225–1233 <https://doi.org/10.1038/sj.bjc.6604017>
- 12 Schick, U., Kyula, J., Barker, H., Patel, R., Zaidi, S., Gregory, C. et al. (2015) Trametinib radiosensitises RAS- and BRAF-mutated melanoma by perturbing cell cycle and inducing senescence. *Radiother. Oncol.* **117**, 364–375 <https://doi.org/10.1016/j.radonc.2015.06.026>
- 13 Yoshida, A., Lee, E.K. and Diehl, J.A. (2016) Induction of therapeutic senescence in vemurafenib-resistant melanoma by extended inhibition of CDK4/6. *Cancer Res.* **76**, 2990–3002 <https://doi.org/10.1158/0008-5472.CAN-15-2931>
- 14 Acosta, J.C. and Gil, J. (2012) Senescence: a new weapon for cancer therapy. *Trends Cell Biol.* **22**, 211–219 <https://doi.org/10.1016/j.tcb.2011.11.006>
- 15 Giuliano, S., Ohanna, M., Ballotti, R. and Bertolotto, C. (2011) Advances in melanoma senescence and potential clinical application. *Pigment Cell Melanoma Res.* **24**, 295–308 <https://doi.org/10.1111/j.1755-148X.2010.00820.x>
- 16 Chicas, A., Wang, X., Zhang, C., McCurrach, M., Zhao, Z., Mert, O. et al. (2010) Dissecting the unique role of the retinoblastoma tumor suppressor during cellular senescence. *Cancer Cell* **17**, 376–387 <https://doi.org/10.1016/j.ccr.2010.01.023>
- 17 Lecot, P., Alimirah, F., Desprez, P.Y., Campisi, J. and Wiley, C. (2016) Context-dependent effects of cellular senescence in cancer development. *Br. J. Cancer* **114**, 1180–1184 <https://doi.org/10.1038/bjc.2016.115>
- 18 Faget, D.V., Ren, Q. and Stewart, S.A. (2019) Unmasking senescence: context-dependent effects of SASP in cancer. *Nat. Rev. Cancer* **19**, 439–453 <https://doi.org/10.1038/s41568-019-0156-2>
- 19 Demaria, M., O’Leary, M.N., Chang, J., Shao, L., Liu, S., Alimirah, F. et al. (2017) Cellular senescence promotes adverse effects of chemotherapy and cancer relapse. *Cancer Discov.* **7**, 165–176 <https://doi.org/10.1158/2159-8290.CD-16-0241>
- 20 Meng, Y., Efimova, E.V., Hamzeh, K.W., Darga, T.E., Mauceri, H.J., Fu, Y.X. et al. (2012) Radiation-inducible immunotherapy for cancer: senescent tumor cells as a cancer vaccine. *Mol. Ther.* **20**, 1046–1055 <https://doi.org/10.1038/mt.2012.19>
- 21 Ohanna, M., Cheli, Y., Bonet, C., Bonazzi, V.F., Allegra, M., Giuliano, S. et al. (2013) Secretome from senescent melanoma engages the STAT3 pathway to favor reprogramming of naive melanoma towards a tumor-initiating cell phenotype. *Oncotarget* **4**, 2212–2224 <https://doi.org/10.18632/oncotarget.1143>
- 22 Liu, Y., Hawkins, O.E., Su, Y., Vilgelm, A.E., Sobolik, T., Thu, Y.M. et al. (2013) Targeting aurora kinases limits tumour growth through DNA damage-mediated senescence and blockade of NF- $\kappa$ B impairs this drug-induced senescence. *EMBO Mol. Med.* **5**, 149–166 <https://doi.org/10.1002/emmm.201201378>
- 23 Vilgelm, A.E., Johnson, C.A., Prasad, N., Yang, J., Chen, S.C., Ayers, G.D. et al. (2016) Connecting the dots: therapy-induced senescence and a tumor-suppressive immune microenvironment. *J. Natl Cancer Inst.* **108**, djv406 <https://doi.org/10.1093/jnci/djv406>
- 24 Lee, S. and Schmitt, C.A. (2019) The dynamic nature of senescence in cancer. *Nat. Cell Biol.* **21**, 94–101 <https://doi.org/10.1038/s41556-018-0249-2>
- 25 Pérez-Mancera, P.A., Young, A.R. and Narita, M. (2014) Inside and out: the activities of senescence in cancer. *Nat. Rev. Cancer* **14**, 547–558 <https://doi.org/10.1038/nrc3773>

- 26 Kaplon, J., Zheng, L., Meissl, K., Chaneton, B., Selivanov, V.A., Mackay, G. et al. (2013) A key role for mitochondrial gatekeeper pyruvate dehydrogenase in oncogene-induced senescence. *Nature* **498**, 109–112 <https://doi.org/10.1038/nature12154>
- 27 Quijano, C., Cao, L., Fergusson, M.M., Romero, H., Liu, J., Gutkind, S. et al. (2012) Oncogene-induced senescence results in marked metabolic and bioenergetic alterations. *Cell Cycle* **11**, 1383–1392 <https://doi.org/10.4161/cc.19800>
- 28 Takebayashi, S., Tanaka, H., Hino, S., Nakatsu, Y., Igata, T., Sakamoto, A. et al. (2015) Retinoblastoma protein promotes oxidative phosphorylation through upregulation of glycolytic genes in oncogene-induced senescent cells. *Aging Cell* **14**, 689–697 <https://doi.org/10.1111/acel.12351>
- 29 Dörr, J.R., Yu, Y., Milanovic, M., Beuster, G., Zasada, C., Däbritz, J.H. et al. (2013) Synthetic lethal metabolic targeting of cellular senescence in cancer therapy. *Nature* **501**, 421–425 <https://doi.org/10.1038/nature12437>
- 30 Hutter, E., Renner, K., Pfister, G., Stöckl, P., Jansen-Dürr, P. and Gnaiger, E. (2004) Senescence-associated changes in respiration and oxidative phosphorylation in primary human fibroblasts. *Biochem. J.* **380**, 919–928 <https://doi.org/10.1042/bj20040095>
- 31 Kamogashira, T., Hayashi, K., Fujimoto, C., Iwasaki, S. and Yamasoba, T. (2017) Functionally and morphologically damaged mitochondria observed in auditory cells under senescence-inducing stress. *NPJ Aging Mech. Dis.* **3**, 2 <https://doi.org/10.1038/s41514-017-0002-2>
- 32 Zwierschke, W., Mazurek, S., Stöckl, P., Hütter, E., Eigenbrodt, E. and Jansen-Dürr, P. (2003) Metabolic analysis of senescent human fibroblasts reveals a role for AMP in cellular senescence. *Biochem. J.* **376**, 403–411 <https://doi.org/10.1042/bj20030816>
- 33 Haq, R., Shoag, J., Andreu-Perez, P., Yokoyama, S., Edelman, H., Rowe, G.C. et al. (2013) Oncogenic BRAF regulates oxidative metabolism via PGC1 $\alpha$  and MITF. *Cancer Cell* **23**, 302–315 <https://doi.org/10.1016/j.ccr.2013.02.003>
- 34 Roesch, A., Vultur, A., Bogeski, I., Wang, H., Zimmermann, K.M., Speicher, D. et al. (2013) Overcoming intrinsic multidrug resistance in melanoma by blocking the mitochondrial respiratory chain of slow-cycling JARID1B(high) cells. *Cancer Cell* **23**, 811–825 <https://doi.org/10.1016/j.ccr.2013.05.003>
- 35 Vazquez, F., Lim, J.-H., Chim, H., Bhalla, K., Gimun, G., Pierce, K. et al. (2013) PGC1 $\alpha$  expression defines a subset of human melanoma tumors with increased mitochondrial capacity and resistance to oxidative stress. *Cancer Cell* **23**, 287–301 <https://doi.org/10.1016/j.ccr.2012.11.020>
- 36 Zhang, G., Frederick, D.T., Wu, L., Wei, Z., Krepler, C., Srinivasan, S. et al. (2016) Targeting mitochondrial biogenesis to overcome drug resistance to MAPK inhibitors. *J. Clin. Invest.* **126**, 1834–1856 <https://doi.org/10.1172/JCI82661>
- 37 Liesa, M. and Shirihai, O.S. (2013) Mitochondrial dynamics in the regulation of nutrient utilization and energy expenditure. *Cell Metab.* **17**, 491–506 <https://doi.org/10.1016/j.cmet.2013.03.002>
- 38 Mishra, P. and Chan, D.C. (2016) Metabolic regulation of mitochondrial dynamics. *J. Cell Biol.* **212**, 379–387 <https://doi.org/10.1083/jcb.201511036>
- 39 Marchesi, F., Turriziani, M., Tortorelli, G., Avisati, G., Torino, F. and De Vecchis, L. (2007) Triazene compounds: mechanism of action and related DNA repair systems. *Pharmacol. Res.* **56**, 275–287 <https://doi.org/10.1016/j.phrs.2007.08.003>
- 40 Dimri, G.P., Lee, X., Basile, G., Acosta, M., Scott, G., Roskelley, C. et al. (1995) A biomarker that identifies senescent human cells in culture and in aging skin in vivo. *Proc. Natl Acad. Sci. U.S.A.* **92**, 9363–9367 <https://doi.org/10.1073/pnas.92.20.9363>
- 41 Merkus, H.G. (2009) *Particle Size Measurements: Fundamentals, Practice, Quality*, Springer Science & Business Media
- 42 Losón, O.C., Song, Z., Chen, H. and Chan, D.C. (2013) Fis1, Mff, Mid49, and Mid51 mediate Drp1 recruitment in mitochondrial fission. *Mol. Biol. Cell* **24**, 659–667 <https://doi.org/10.1091/mbc.e12-10-0721>
- 43 Pagliuso, A., Tham, T.N., Stevens, J.K., Lagache, T., Persson, R., Salles, A. et al. (2016) A role for septin 2 in Drp1-mediated mitochondrial fission. *EMBO Rep.* **17**, 858–873 <https://doi.org/10.15252/embr.201541612>
- 44 Park, Y.Y., Lee, S., Karbowski, M., Neutzner, A., Youle, R.J. and Cho, H. (2010) Loss of MARCH5 mitochondrial E3 ubiquitin ligase induces cellular senescence through dynamin-related protein 1 and mitofusin 1. *J. Cell Sci.* **123**, 619–626 <https://doi.org/10.1242/jcs.061481>
- 45 Song, W., Bossy, B., Martin, O.J., Hicks, A., Lubitz, S., Knott, A.B. et al. (2008) Assessing mitochondrial morphology and dynamics using fluorescence wide-field microscopy and 3D image processing. *Methods* **46**, 295–303 <https://doi.org/10.1016/j.ymeth.2008.10.003>
- 46 Brand, M. and Nicholls, D. (2011) Assessing mitochondrial dysfunction in cells. *Biochem. J.* **435**, 297–312 <https://doi.org/10.1042/BJ20110162>
- 47 Salabei, J.K., Gibb, A.A. and Hill, B.G. (2014) Comprehensive measurement of respiratory activity in permeabilized cells using extracellular flux analysis. *Nat. Protoc.* **9**, 421–438 <https://doi.org/10.1038/nprot.2014.018>
- 48 Nicholls, D.G. and Ferguson, S.J. (2013) *Bioenergetics*, Elsevier Ltd
- 49 Wu, M., Neilson, A., Swift, A.L., Moran, R., Tamagnine, J., Parslow, D. et al. (2007) Multiparameter metabolic analysis reveals a close link between attenuated mitochondrial bioenergetic function and enhanced glycolysis dependency in human tumor cells. *Am. J. Physiol. Cell Physiol.* **292**, C125–C136 <https://doi.org/10.1152/ajpcell.00247.2006>
- 50 Costes, S.V., Daelemans, D., Cho, E.H., Dobbin, Z., Pavlakis, G. and Lockett, S. (2004) Automatic and quantitative measurement of protein-protein colocalization in live cells. *Biophys. J.* **86**, 3993–4003 <https://doi.org/10.1529/biophysj.103.038422>
- 51 Dunn, K.W., Kamočka, M.M. and McDonald, J.H. (2011) A practical guide to evaluating colocalization in biological microscopy. *Am. J. Physiol. Cell Physiol.* **300**, C723–C742 <https://doi.org/10.1152/ajpcell.00462.2010>
- 52 Zhang, H., Maguire, D., Swarts, S., Sun, W., Yang, S., Wang, W. et al. (2009) Replication of murine mitochondrial DNA following irradiation. *Adv. Exp. Med. Biol.* **645**, 43–48 [https://doi.org/10.1007/978-0-387-85998-9\\_7](https://doi.org/10.1007/978-0-387-85998-9_7)
- 53 Gorbunova, V., Seluanov, A. and Pereira-Smith, O.M. (2003) Evidence that high telomerase activity may induce a senescent-like growth arrest in human fibroblasts. *J. Biol. Chem.* **278**, 7692–7698 <https://doi.org/10.1074/jbc.M212944200>
- 54 Livak, K.J. and Schmittgen, T.D. (2001) Analysis of relative gene expression data using real-time quantitative PCR and the 2<sup>-</sup>(Delta Delta C(T)) method. *Methods* **25**, 402–408 <https://doi.org/10.1006/meth.2001.1262>
- 55 Eigenter, A., Draxl, A., Wiethüchter, A., Kuznetsov, A., Lassing, B. and Gnaiger, E. (2012) Laboratory protocol: citrate synthase, a mitochondrial marker enzyme. *Mitochondrial Physiol. Netw.* **17**, 1–11
- 56 Sarbassov, D.D., Guertin, D.A., Ali, S.M. and Sabatini, D.M. (2005) Phosphorylation and regulation of Akt/PKB by the rictor-mTOR complex. *Science* **307**, 1098–1101 <https://doi.org/10.1126/science.1106148>
- 57 Stewart, S.A., Dykxhoorn, D.M., Palliser, D., Mizuno, H., Yu, E.Y., An, D.S. et al. (2003) Lentivirus-delivered stable gene silencing by RNAi in primary cells. *RNA* **9**, 493–501 <https://doi.org/10.1261/rna.2192803>
- 58 Ruiz, L.M., Jensen, E.L., Rossel, Y., Puaș, G.I., Gonzalez-Ibanez, A.M., Bustos, R.I. et al. (2016) Non-cytotoxic copper overload boosts mitochondrial energy metabolism to modulate cell proliferation and differentiation in the human erythroleukemic cell line K562. *Mitochondrion* **29**, 18–30 <https://doi.org/10.1016/j.mito.2016.04.005>

- 59 Melnikova, V.O., Bolshakov, S.V., Walker, C. and Ananthaswamy, H.N. (2004) Genomic alterations in spontaneous and carcinogen-induced murine melanoma cell lines. *Oncogene* **23**, 2347–2356 <https://doi.org/10.1038/sj.onc.1207405>
- 60 Gilant, E., Kaza, M., Szlagowska, A., Serafin-Byczak, K. and Rudzki, P.J. (2011) Validated HPLC method for determination of temozolomide in human plasma. *Acta Pol. Pharm.* **69**, 1347–1355 PMID:23285701
- 61 Patel, M., McCully, C., Godwin, K. and Balis, F.M. (2003) Plasma and cerebrospinal fluid pharmacokinetics of intravenous temozolomide in non-human primates. *J. Neuro. Oncol.* **61**, 203–207 <https://doi.org/10.1023/A:1022592913323>
- 62 Lener, B., Koziol, R., Pircher, H., Hütter, E., Greussing, R., Herndler-Brandstetter, D. et al. (2009) The NADPH oxidase Nox4 restricts the replicative lifespan of human endothelial cells. *Biochem. J.* **423**, 363–374 <https://doi.org/10.1042/BJ20090666>
- 63 Weyemi, U., Lagente-Chevallier, O., Boufrajeh, M., Prenois, F., Courtin, F., Caillou, B. et al. (2012) ROS-generating NADPH oxidase NOX4 is a critical mediator in oncogenic H-Ras-induced DNA damage and subsequent senescence. *Oncogene* **31**, 1117–1129 <https://doi.org/10.1038/ncr.2011.327>
- 64 Robin, E.D. and Wong, R. (1988) Mitochondrial DNA molecules and virtual number of mitochondria per cell in mammalian cells. *J. Cell. Physiol.* **136**, 507–513 <https://doi.org/10.1002/jcp.1041360316>
- 65 Reisch, A.S. and Elpeleg, O. (2007) Biochemical assays for mitochondrial activity: assays of TCA cycle enzymes and PDHc. *Methods Cell Biol.* **80**, 199–222 [https://doi.org/10.1016/S0091-679X\(06\)80010-5](https://doi.org/10.1016/S0091-679X(06)80010-5)
- 66 Clayton, D.A. (1992) Transcription and replication of animal mitochondrial DNAs. *Int. Rev. Cytol.* **141**, 217–232 [https://doi.org/10.1016/S0074-7696\(08\)62067-7](https://doi.org/10.1016/S0074-7696(08)62067-7)
- 67 Wu, Z., Puigserver, P., Andersson, U., Zhang, C., Adelmant, G., Mootha, V. et al. (1999) Mechanisms controlling mitochondrial biogenesis and respiration through the thermogenic coactivator PGC-1. *Cell* **98**, 115–124 [https://doi.org/10.1016/S0092-8674\(00\)80611-X](https://doi.org/10.1016/S0092-8674(00)80611-X)
- 68 Cherok, E., Xu, S., Li, S., Das, S., Meltzer, W.A., Zalzman, M. et al. (2017) Novel regulatory roles of Mff and Drp1 in E3 ubiquitin ligase MARCH5-dependent degradation of MiD49 and Mcl1 and control of mitochondrial dynamics. *Mol. Biol. Cell* **28**, 396–410 <https://doi.org/10.1091/mbc.e16-04-0208>
- 69 Ducommun, S., Deak, M., Sumpton, D., Ford, R.J., Núñez Galindo, A., Kussmann, M. et al. (2015) Motif affinity and mass spectrometry proteomic approach for the discovery of cellular AMPK targets: identification of mitochondrial fission factor as a new AMPK substrate. *Cell. Signal.* **27**, 978–988 <https://doi.org/10.1016/j.cellsig.2015.02.008>
- 70 Gandre-Babbe, S. and van der Blik, A.M. (2008) The novel tail-anchored membrane protein Mff controls mitochondrial and peroxisomal fission in mammalian cells. *Mol. Biol. Cell* **19**, 2402–2412 <https://doi.org/10.1091/mbc.e07-12-1287>
- 71 Toyama, E.Q., Herzig, S., Courchet, J., Lewis, Jr, T.L., Loson, O.C., Hellberg, K. et al. (2016) Metabolism. AMP-activated protein kinase mediates mitochondrial fission in response to energy stress. *Science* **351**, 275–281 <https://doi.org/10.1126/science.aab4138>
- 72 UniProt Consortium. (2019) Uniprot: a worldwide hub of protein knowledge. *Nucleic Acids Res.* **47**, D506–D515 <https://doi.org/10.1093/nar/gky1049>
- 73 Otera, H., Wang, C., Cleland, M.M., Setoguchi, K., Yokota, S., Youle, R.J. et al. (2010) Mff is an essential factor for mitochondrial recruitment of Drp1 during mitochondrial fission in mammalian cells. *J. Cell Biol.* **191**, 1141–1158 <https://doi.org/10.1083/jcb.201007152>
- 74 Liu, R. and Chan, D.C. (2015) The mitochondrial fission receptor Mff selectively recruits oligomerized Drp1. *Mol. Biol. Cell* **26**, 4466–4477 <https://doi.org/10.1091/mbc.E15-08-0591>
- 75 Oliva, C.R., Nozell, S.E., Diers, A., McClugage, S.G., Sarkaria, J.N., Markert, J.M. et al. (2010) Acquisition of temozolomide chemoresistance in gliomas leads to remodeling of mitochondrial electron transport chain. *J. Biol. Chem.* **285**, 39759–39767 <https://doi.org/10.1074/jbc.M110.147504>
- 76 Cairns, R.A., Harris, I.S. and Mak, T.W. (2011) Regulation of cancer cell metabolism. *Nat. Rev. Cancer* **11**, 85–95 <https://doi.org/10.1038/nrc2981>
- 77 DeBerardinis, R.J., Lum, J.J., Hatzivassiliou, G. and Thompson, C.B. (2008) The biology of cancer: metabolic reprogramming fuels cell growth and proliferation. *Cell Metab.* **7**, 11–20 <https://doi.org/10.1016/j.cmet.2007.10.002>
- 78 Warburg, O.H. (1930) *Metabolism of Tumours*, Constable, London
- 79 Wiley, C.D., Velarde, M.C., Lecot, P., Liu, S., Sarnoski, E.A., Freund, A. et al. (2016) Mitochondrial dysfunction induces senescence with a distinct secretory phenotype. *Cell Metab.* **23**, 303–314 <https://doi.org/10.1016/j.cmet.2015.11.011>
- 80 LeBleu, V.S., O'Connell, J.T., Gonzalez Herrera, K.N., Wikman, H., Pantel, K., Haigis, M.C. et al. (2014) PGC-1 $\alpha$  mediates mitochondrial biogenesis and oxidative phosphorylation in cancer cells to promote metastasis. *Nat. Cell Biol.* **16**, 992–1003, 1001–1015 <https://doi.org/10.1038/ncb3039>
- 81 Shen, Q., Yamano, K., Head, B.P., Kawajiri, S., Cheung, J.T., Wang, C. et al. (2014) Mutations in Fis1 disrupt orderly disposal of defective mitochondria. *Mol. Biol. Cell* **25**, 145–159 <https://doi.org/10.1091/mbc.e13-09-0525>
- 82 Lavie, J., De Belvalet, H., Sonon, S., Ion, A.M., Dumon, E., Melsner, S. et al. (2018) Ubiquitin-dependent degradation of mitochondrial proteins regulates energy metabolism. *Cell Rep.* **23**, 2852–2863 <https://doi.org/10.1016/j.celrep.2018.05.013>
- 83 Taanman, J.W. (1997) Human cytochrome c oxidase: structure, function, and deficiency. *J. Bioenerg. Biomembr.* **29**, 151–163 <https://doi.org/10.1023/A:1022638013825>
- 84 Kunz, W.S., Kudin, A., Vielhaber, S., Elger, C.E., Attardi, G. and Villani, G. (2000) Flux control of cytochrome c oxidase in human skeletal muscle. *J. Biol. Chem.* **275**, 27741–27745 <https://doi.org/10.1074/jbc.M004833200>
- 85 Letellier, T., Heinrich, R., Malgat, M. and Mazat, J.P. (1994) The kinetic basis of threshold effects observed in mitochondrial diseases: a systemic approach. *Biochem. J.* **302**, 171–174 <https://doi.org/10.1042/bj3020171>
- 86 Soriano, F.X., Liesa, M., Bach, D., Chan, D.C., Palacin, M. and Zorzano, A. (2006) Evidence for a mitochondrial regulatory pathway defined by peroxisome proliferator-activated receptor-gamma coactivator-1 alpha, estrogen-related receptor-alpha, and mitofusin 2. *Diabetes* **55**, 1783–1791 <https://doi.org/10.2337/db05-0509>
- 87 Mitra, K., Wunder, C., Roysam, B., Lin, G. and Lippincott-Schwartz, J. (2009) A hyperfused mitochondrial state achieved at G1-S regulates cyclin E buildup and entry into S phase. *Proc. Natl Acad. Sci. U.S.A.* **106**, 11960–11965 <https://doi.org/10.1073/pnas.0904875106>
- 88 Tondera, D., Grandemange, S., Jourdain, A., Karbowski, M., Mattenberger, Y., Herzig, S. et al. (2009) SLP-2 is required for stress-induced mitochondrial hyperfusion. *EMBO J.* **28**, 1589–1600 <https://doi.org/10.1038/emboj.2009.89>
- 89 Gomes, L.C., Di Benedetto, G. and Scorrano, L. (2011) During autophagy mitochondria elongate, are spared from degradation and sustain cell viability. *Nat. Cell Biol.* **13**, 589–598 <https://doi.org/10.1038/ncb2220>
- 90 Yao, C.H., Wang, R., Wang, Y., Kung, C.P., Weber, J.D. and Patti, G.J. (2019) Mitochondrial fusion supports increased oxidative phosphorylation during cell proliferation. *eLife* **8**, e41351 <https://doi.org/10.7554/eLife.41351>

- 91 Bulthuis, E.P., Adjobo-Hermans, M.J.W., Willems, P. and Koopman, W.J.H. (2018) Mitochondrial morphofunction in mammalian cells. *Antioxid. Redox Signal.* **30**, 2066–2109 <https://doi.org/10.1089/ars.2018.7534>
- 92 Sauvanet, C., Duvezin-Caubet, S., di Rago, J.P. and Rojo, M. (2010) Energetic requirements and bioenergetic modulation of mitochondrial morphology and dynamics. *Semin. Cell Dev. Biol.* **21**, 558–565 <https://doi.org/10.1016/j.semcdb.2009.12.006>
- 93 Yoon, Y.S., Yoon, D.S., Lim, I.K., Yoon, S.H., Chung, H.Y., Rojo, M. et al. (2006) Formation of elongated giant mitochondria in DFO-induced cellular senescence: involvement of enhanced fusion process through modulation of Fis1. *J. Cell. Physiol.* **209**, 468–480 <https://doi.org/10.1002/jcp.20753>
- 94 Lee, S., Jeong, S.-Y., Lim, W.-C., Kim, S., Park, Y.-Y., Sun, X. et al. (2007) Mitochondrial fission and fusion mediators, hFis1 and OPA1, modulate cellular senescence. *J. Biol. Chem.* **282**, 22977–22983 <https://doi.org/10.1074/jbc.M700679200>
- 95 Sharpless, N.E. and Sherr, C.J. (2015) Forging a signature of in vivo senescence. *Nat. Rev. Cancer* **15**, 397–408 <https://doi.org/10.1038/nrc3960>
- 96 Freyer, J.P. (1998) Decreased mitochondrial function in quiescent cells isolated from multicellular tumor spheroids. *J. Cell Physiol.* **176**, 138–149 [https://doi.org/10.1002/\(SICI\)1097-4652\(199807\)176:1<138::AID-JCP16>3.0.CO;2-3](https://doi.org/10.1002/(SICI)1097-4652(199807)176:1<138::AID-JCP16>3.0.CO;2-3)
- 97 Aulestia, F.J., Néant, I., Dong, J., Haiech, J., Kilhoffer, M.C., Moreau, M. et al. (2018) Quiescence status of glioblastoma stem-like cells involves remodelling of Ca<sup>2+</sup> signalling and mitochondrial shape. *Sci. Rep.* **8**, 9731 <https://doi.org/10.1038/s41598-018-28157-8>
- 98 Filadi, R., Pendin, D. and Pizzo, P. (2018) Mitofusin 2: from functions to disease. *Cell Death Dis.* **9**, 330 <https://doi.org/10.1038/s41419-017-0023-6>
- 99 Ichinohe, T., Yamazaki, T., Koshiba, T. and Yanagi, Y. (2013) Mitochondrial protein mitofusin 2 is required for NLRP3 inflammasome activation after RNA virus infection. *Proc. Natl Acad. Sci. U.S.A.* **110**, 17963–17968 <https://doi.org/10.1073/pnas.1312571110>
- 100 Acosta, J.C., Banito, A., Wuestefeld, T., Georgilis, A., Janich, P., Morton, J.P. et al. (2013) A complex secretory program orchestrated by the inflammasome controls paracrine senescence. *Nat. Cell Biol.* **15**, 978–990 <https://doi.org/10.1038/ncb2784>
- 101 Robbins, P.D. and Niedernhofer, L.J. (2017) Advances in therapeutic approaches to extend healthspan: a perspective from the 2(nd) Scripps symposium on the biology of aging. *Aging Cell* **16**, 610–614 <https://doi.org/10.1111/accel.12620>
- 102 Zhu, Y., Tchkonja, T., Pirtskhalava, T., Gower, A.C., Ding, H., Giorgadze, N. et al. (2015) The Achilles' heel of senescent cells: from transcriptome to senolytic drugs. *Aging Cell* **14**, 644–658 <https://doi.org/10.1111/accel.12344>
- 103 Samaraweera, L., Adomako, A., Rodriguez-Gabin, A. and McDaid, H.M. (2017) A novel indication for panobinostat as a senolytic drug in NSCLC and HNSCC. *Sci. Rep.* **7**, 1900 <https://doi.org/10.1038/s41598-017-01964-1>
- 104 Correia-Melo, C., Marques, F.D., Anderson, R., Hewitt, G., Hewitt, R., Cole, J. et al. (2016) Mitochondria are required for pro-ageing features of the senescent phenotype. *EMBO J.* **35**, 724–742 <https://doi.org/10.15252/embj.201592862>